THESIS FOR THE DEGREE OF LICENTIATE OF ENGINEERING

High-resolution radio imaging of galaxy nuclei

ESKIL VARENIUS

CHALMERS

Department of Earth and Space Sciences
CHALMERS UNIVERSITY OF TECHNOLOGY
Göteborg, Sweden 2014

High-resolution radio imaging of galaxy nuclei
ESKIL VARENIUS

Radio Astronomy & Astrophysics Group
Department of Earth and Space Sciences
Chalmers University of Technology
SE–412 96 Göteborg, Sweden
Phone: +46 (0)31–772 1000

Contact information:
Eskil Varenius
Onsala Space Observatory
Chalmers University of Technology
SE–439 92 Onsala, Sweden

Phone: +46 (0)31–772 5545
Fax: +46 (0)31–772 5590
Email: eskil.varenius@chalmers.se

Cover image:
Composite of four images. Bottom-right and center: the 25m radio telescope at Onsala Space Observatory. The remaining three images were made with radio telescopes as part of this thesis, each showing a small part of a galaxy nucleus in pseudo-colors. Bottom-left: The galaxy NGC 4418, which is surprisingly weak at radio wavelengths despite being very luminous at infrared wavelengths. Top-left: The galaxy M82 as seen at 154 Mhz with the international LOFAR telescope - a new world record in image resolution at low frequencies. Top-right: The western nucleus of the interacting galaxy Arp 220, as seen at 5 GHz using telescopes all over the earth, hosting over 40 radio supernovae or supernova remnants, telling us about the physics of star formation. Image credits: Onsala Space Observatory/Roger Hammargren, Eskil Varenius, and Simon Farsi.

Printed by Chalmers Reproservice
Chalmers University of Technology
Göteborg, Sweden 2014

High-resolution radio imaging of galaxy nuclei

ESKIL VARENIUS
Department of Earth and Space Sciences
Chalmers University of Technology

Abstract

Star formation and galaxy evolution are intimately linked together. A detailed understanding of the environment where stars form may help us explain the differences we see between galaxies today and at earlier times in the history of the Universe. Galaxy nuclei are often heavily obscured by dust and cannot be observed in detail at optical wavelengths. Since radio waves are almost unaffected by dust, they can tell us about the physics in dense star forming regions.
To achieve high enough image resolution at radio wavelengths, we use interferometry to synthesize a large aperture using data from multiple radio telescopes. We obtain detailed images of radio sources associated with star formation, such as core-collapse supernovae and their corresponding remnants. Using series of images at different observing wavelengths and different times, we can model the evolution of the radio sources and estimate densities, magnetic fields and star formation rates.
We have studied the luminous nuclei of three different galaxies; M82, NGC 4418 and Arp 220. M82 and Arp 220 are well known starburst galaxies, meaning they have rates of star formation so high that they cannot be sustained over the history of the Universe. Both galaxies also follow the well-known FIR/radio correlation. In this thesis, I present ongoing work to model in detail the environment of Arp 220 and M82, based on high-resolution imaging of their nuclei. Our image of M82 is a new record in terms of image resolution at low frequencies. NGC 4418 is different; it does not follow the FIR/radio correlation. The high observed excess infrared luminosity of this galaxy has been suggested to come instead from an accreting black hole. We argue that although there might be an accreting black hole in NGC 4418, it cannot account for all the complex structure revealed by high-resolution radio imaging, indicating a significant starburst component.

Keywords: galaxies: starburst - galaxies: active - galaxies: individual: Arp 220, M82, NGC 4418 - techniques: high angular resolution - stars: supernovae - radio continuum: galaxies

Research contributions

This thesis is based on the work contained in **Paper** I**:**

- E. Varenius, J. E. Conway, I. Martí-Vidal, S. Aalto, R. Beswick, F. Costagliola, and H.-R. Klöckner
  The radio core structure of the luminous infrared galaxy NGC 4418
  Accepted 13 February 2014 for publication in Astronomy & Astrophysics.

Ongoing research projects which have been a major part of this work, but are not discussed in Paper I, are described in chapters 4 and 5.

Acknowledgements

This thesis would not have been possible without the kind assistance of many people, especially my three supervisors. First, I want to thank John Conway for being a great source of inspiration and for introducing me to the wonderful world of corrugated roofs. You have an infinite supply of good ideas and an amazing memory - I have really learned a lot from you! Next I want to thank Ivan Martí-Vidal for your everlasting good humor, for your broad and profound knowledge of interferometry, and for gladly sharing all of this with me at any time. If we ever get bored in Onsala, let us find out if there is a duet for trumpet and tuba that we both would like to play! Last but not least I want to thank Susanne Aalto for always believing in me, for an impressive knowledge of galaxies in all shapes and forms, and for many interesting discussions about leadership and science. I look forward to working with you more in the years to come, and I hope I will find time soon to learn more about astrochemistry and spectral lines!

Life in Onsala would be a lot less inspiring and fun without all my fellow PhD students and other friends here. Thank you for all nice discussions in the space bus, and for being an excellent film crew! A special thanks to Fabien Batejat for helping me through my first adventures in the world of AIPS, for being a very nice room mate, and for teaching me how to play Babyfoot properly (although I might need to refresh the rules before going to Chile next time). I will miss you in Onsala, and you are welcome to join me for a game of recycling whenever you wish!

This work could surely not have been done without help of computers. Since computers are people too, I want to thank Roger Hammargren and Simon Casey in particular for convincing the overgrown calculators in the server room to speak ParselTongue properly.

I am also fully convinced of that nothing in Onsala would work for many minutes without Paula Rosell keeping track of us all - without you we would all be lost - Thank you!

I also want to thank Rodrigo Parra for inviting me to his home in Santiago, Nick Wrigley for good company in the New Mexico desert, and Neil Jackson for knowing the best place to get pancakes in Leiden.

Finally, I want to thank my family and friends outside the observatory. You always inspire me to continue forward and to remember the joy of music.

Thank you all!

Eskil

Contents

Chapter 1

Introduction

When we look at the sky with our naked eyes on a clear winter night, we see stars and galaxies. We wonder what and where they are. We might also wonder why some stars twinkle. The reason they do is because the starlight travels not only through space, but also has to cross the Earth's atmosphere. The atmosphere affects, in some way, almost all light passing through it. How much the light from space is disturbed by the atmosphere depends on the wavelength (color) of the light. For optical wavelengths (light we see with our eyes) this effect is not larger than what we see as twinkling stars [1]. However, not all wavelengths can pass through the atmosphere. Most wavelengths are absorbed or heavily scattered before reaching us at the surface. Therefore, a very large fraction of the information available to us about space is unfortunately lost on its way down through the atmosphere. An obvious solution to this is to launch telescopes into space, above the Earth's atmosphere. This has been done and it is the only way to detect X-rays and to make sharp images at infrared wavelengths. However, launching things into space is very challenging and there are limits also to what satellites can do. Luckily, there are other wavelengths than visible light for which the atmosphere is transparent (see Fig. 1.1).

We see in Fig. 1.1 that visible light pass all the way down to the Earth. But also radio waves, i.e. light of centimeter and meter wavelengths, reach us without much disturbance from the atmosphere. This means that if we want to learn more about stars and galaxies, it is a good idea to look not only through optical telescopes but also to use radio telescopes.

[1] The twinkling effect we see with our eyes is in fact severe enough to be the subject of many research projects. People have invented many clever contraptions and computer programs to remove, or at least to some extent correct for, the twinkling effect. These developments are amazing and makes it possible to make very impressive images of the sky at optical wavelengths. Further details on optical imaging are however beyond the scope of this work.

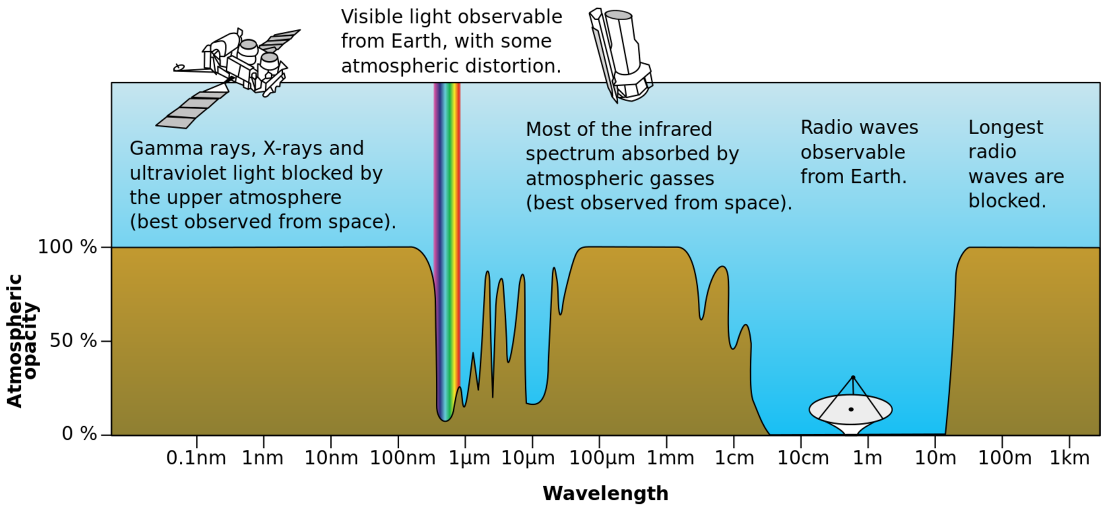

Figure 1.1: Most light from outer space will be blocked by the Earth's atmosphere. Therefore, we can get information about space only at specific wavelength ranges, normally called *windows*. Visible light falls within such a window, as do a few infrared wavelength ranges. There is also very little blocking at radio wavelengths, which is the reason we do radio astronomy. Credit: NASA/IPAC.

Radio telescopes work in a slightly different way than optical telescopes, and they also look different. They are usually large parabolic dishes (see Fig. 1.2) and one cannot look directly through them to see the stars. Instead we use electronics and computers to record signals from space and to make images of the sky. I want to stress that even though one cannot look through a radio telescope directly with the naked eye, it is still possible to make images by means of elaborate data processing, see for example the cover image of this thesis.

1.1 Why do we need radio interferometry?

A high-quality image for an astronomer means two things: deep and sharp. Deep means a low noise, and is important because we want to see faint things such as stars in other galaxies. Sharp is important because we want to learn the shape and form of the objects we study. To get deeper images we can, in principle, just observe for a longer time. One may speed up the process by building more telescopes. Getting sharp images however is a different matter.

Figure 1.2: The Arecibo radio telescope in Puerto Rico. This is the world's largest single dish with a diameter of 300 m. Data from this telescope was used in this thesis work (together with other telescopes) to produce very sharp images of the galaxy Arp 220. Photo courtesy of the NAIC - Arecibo Observatory, a facility of the NSF.

The sharpness, or resolution, of an image depends on the wavelength of the light you choose to observe and the size of your telescope [2]. Because the wavelength of visible light is very short (see Fig. 1.1), an optical telescope of moderate size (~ 1 m) is sufficient to produce images with high enough (subarcsecond) resolution to do science. However, radio waves are much (100 000 times, see Fig, 1.1) longer and therefore we need much larger telescopes to get sharp images. Even the biggest radio telescopes mechanically possible to build (like Arecibo, see Fig. 1.2) are not big enough to compensate for the huge difference

[2]The actual measure of the image resolution in radians is $\theta \approx 1.22\lambda/D$ where λ is the observing wavelength and D is the size of your telescope, or the longest separation in your interferometer. This is the Rayleigh-criterion for the diffraction limit of a circular aperture, i.e. the angular distance between the central maximum and the first minimum in the interference pattern. This is a very common way of defining resolution in astronomy.

in wavelength compared to optical light. Is sharp images at radio wavelengths then technically impossible? No, because we can use a very clever technique called interferometry.

Interferometry is a beautiful and powerful way of combining data from many telescopes to synthesize (emulate) a telescope as large as the distance between the connected telescopes. If we put two telescopes 1 km apart, interferometry gives us as sharp an image as if we would have had a single dish with a diameter of 1 km. In the most extreme case, we can use telescopes all over the world to synthesize a telescope of size 12000 km (diameter of the Earth). In fact, because of less atmospheric turbulence at radio frequencies, we can actually achieve better resolution than possible in most optical telescopes. We call a system of connected telescopes an interferometer. Interferometers truly are wonderful machines.

In this thesis I describe work carried out using several interferometers. At meter wavelengths we use the European Low Frequency ARray (LOFAR). For cm waves we use the Multi-Element Radio Linked Interferometer Network (MERLIN) located in the UK. For the highest possible resolution we use the European VLBI Network (EVN, see Fig. 1.3) together with the Very Long Baseline Array (VLBA) in the USA.

1.2 Why do we study other galaxies?

It is impossible to grasp all details of a single galaxy. Our own galaxy, the Milky Way, is thought to be the home of more than 100 billion stars, and many of these may have planets. The question of how it came to be is a very interesting one, but is hard to solve by studying the Milky Way alone. This is partly because the evolution of galaxies is so slow compared to our lives on Earth that we simply cannot follow a single galaxy for enough time to see it change. But, it is also hard because studying only one galaxy is a bit like studying only one species on Earth and trying to understand the idea of biological evolution. To get more clues we therefore study other galaxies. Some are very different compared to the Milky Way in terms of shape, size and age.

When studying galaxies very far away (and hence far back in time because of the finite speed of light) it is hard to make images sharp enough to see the details, even using interferometry. Therefore, we use statistical and approximate methods to analyze what we see. These methods need, however, first to be carefully checked and calibrated against more nearby galaxies where we can measure both the average properties and the underlying details. In this thesis I describe work carried out to make high-resolution images of three galaxies; Arp 220, M82 and NGC 4418. These galaxies were chosen because they are different in many interesting ways, but still close enough for us to study in detail.

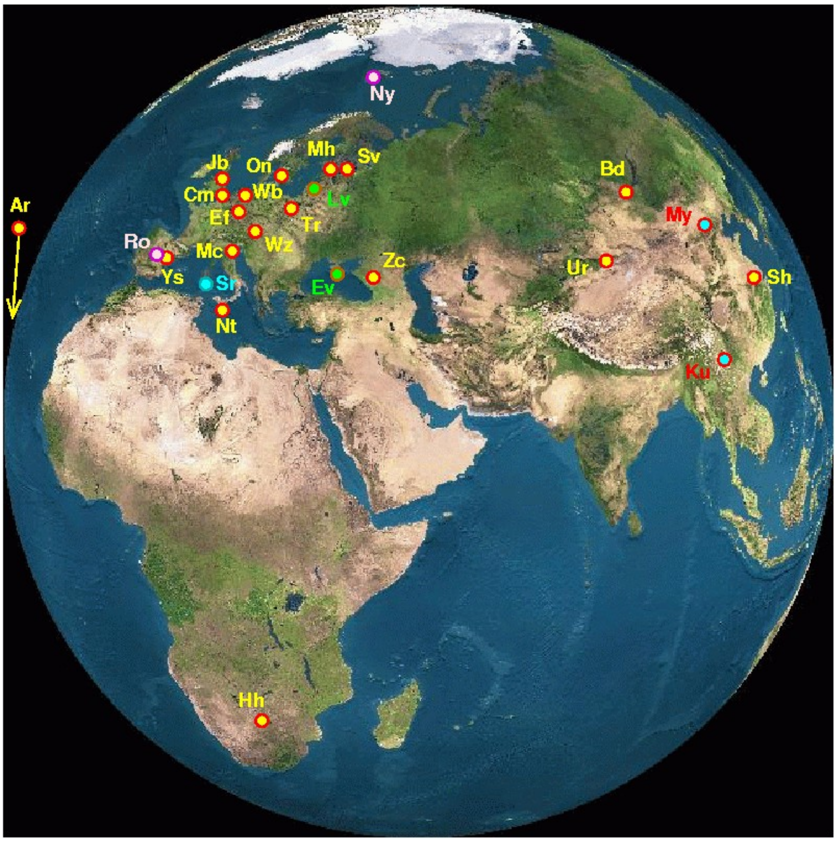

Figure 1.3: The European VLBI Network (EVN) is an interferometric array of radio telescopes spread throughout all over the world. Using many telescopes together, we can obtain high resolution images of cosmic radio sources. The dots and letters on this map marks the location of different telescopes, most of which has been used in this thesis work. Credit: http://www.evlbi.org/.

The work described in this thesis is about making the images, and then interpreting scientifically what we see. The scientific analysis is still ongoing and this thesis will only briefly describe the results of our studies of Arp 220 and M82, whereas our analysis of NGC 4418 is described in more detail in Paper I.

(a)

(b)

(c)

Figure 1.4: Optical images of the three galaxies studied in this thesis: Arp220 (Fig. (a), Credit: R. Thompson (U. Arizona) et al., NICMOS, HST, NASA.), M82 (Fig. (b), Credit: NASA, ESA and the Hubble Heritage Team STScI/AURA). Acknowledgment: J. Gallagher (University of Wisconsin), M. Mountain (STScI) and P. Puxley (NSF)), and NGC 4418 (Fig. (c), Credit: Sakamoto et al. (2013)). These are beautiful images, but to see the very smallest details like the supernovae and to see through the obscured central regions with high resolution, we need to use radio interferometry.

Chapter 2

Radio emission from galaxies

In this work, we have studied radio continuum emission from galaxies. In addition to the continuum, there are many interesting spectral lines present at radio frequencies (such as OH masers or the well known 21 cm hydrogen line) carrying a wealth of interesting information. However, this thesis focuses on imaging the radio continuum and further discussion of spectral line emission and absorption mechanisms is beyond the scope of this work.

2.1 Important electromagnetic interactions

The radio continuum of a star forming galaxy is made up of emission and absorption of photons by charged particles moving in electromagnetic fields. Two very important processes give rise to what is usually referred to as free-free emission and synchrotron emission, and these are briefly described below. A simple model combining free-free emission, absorption and synchrotron emission from Condon (1992) was used in Paper I, to estimate the star formation rate of compact features in the nucleus of the galaxy NGC 4418.

For shorter wavelengths, i.e. the far-infrared, emission from dust grains dominate the spectrum. The relation between free-free, synchrotron and dust can be seen in Fig. 2.1 for the galaxy M82.

2.1.1 Free-free emission and absorption

Free-free emission is produced in electromagnetic interactions between charged particles such as electrons or protons. The term free-free refers to that the particles are not bound in atoms before and after the interaction. Free-free emission is sometimes also referred to as *Brehmsstrahlung*, because deceleration means ”to brake”, or as *thermal* emission, because the distribution of kinetic energies

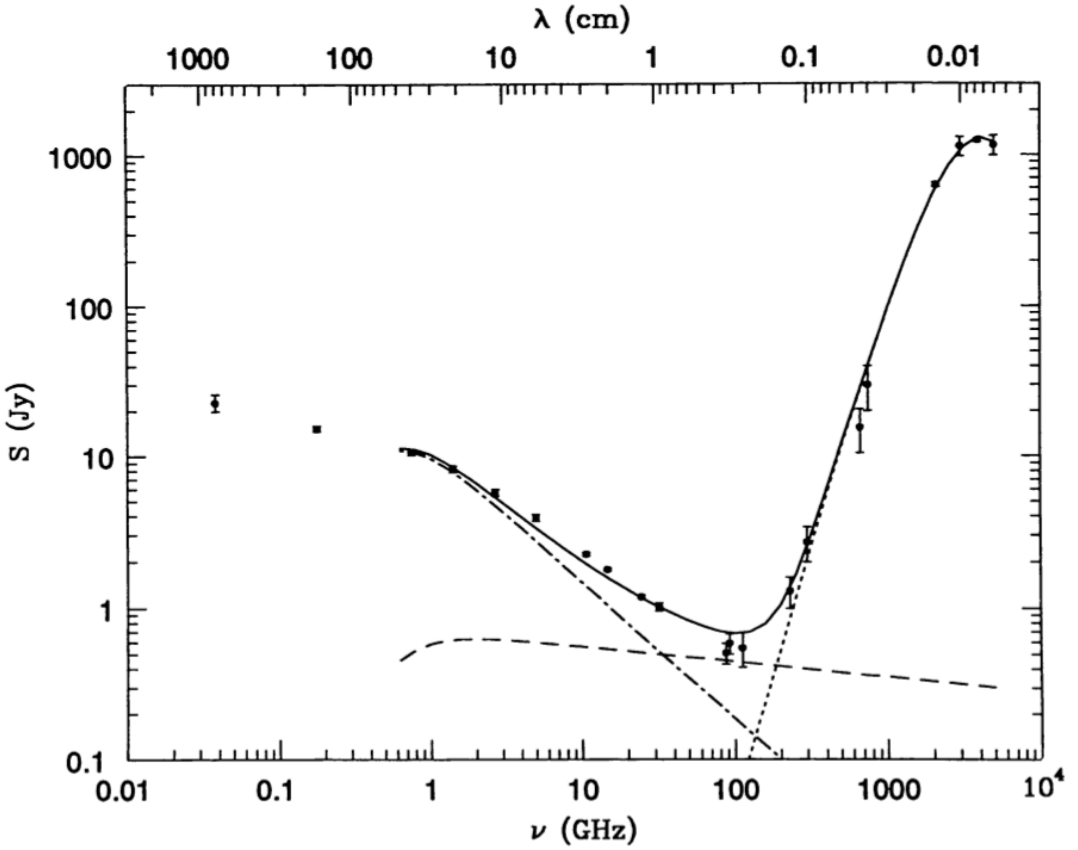

Figure 2.1: The observed radio/FIR spectrum of M82 is the sum (solid line) of synchrotron (dot-dash line), free-free (dashed line) and dust (dotted line) components. The HII regions in this bright starburst galaxy start to become opaque below $\nu \sim 1\,\mathrm{GHz}$, reducing both the free-free and synchrotron flux densities. Thermal re-radiation from dust swamps the radio emission at higher frequencies. Figure from Condon (1992).

of the charged particles can be described by a Boltzmann distribution with some temperature. Free-free emission requires free particles, but the ionizing source does not have to be massive stars. It can also be other energy sources such as accreting black holes. The frequency dependence of the free-free emission at optically thin frequencies can be described by a power-law $S_\nu \propto \nu^{-0.1}$ (see the dashed line in Fig. 2.1).

If, however, the free-free emission is due to star formation, it is a direct measure of the current number of the most massive (and short-lived) stars. These stars emit many photons energetic enough ($h\nu > 13.6eV$) to ionize a large volume of the atomic hydrogen present in the circumstellar medium. Such an ionized region is called a HII-region and can be detected at radio wavelengths. If we assume an initial mass function, it is possible to estimate a total star-formation rate from the measured free-free emission.

The inverse mechanism, called free-free *absorption* means that instead of emitting a photon as a result of the interaction, a photon is absorbed and the energy transferred to the charged particles involved. This effect is very significant at low frequencies and attenuate the radio emission, thereby flattening the radio spectra (below 1 GHz in Fig. 2.1). The spectrum of optically thick HII regions can be described by the power-law $S_\nu \propto \nu^2$.

2.1.2 Synchrotron emission and absorption

Synchrotron emission comes from the acceleration of charged particles moving in a magnetic field, see Fig. 2.2. In star forming galaxies synchrotron emission from supernovae dominates the radio emission below $\nu \sim 30\,\mathrm{GHz}$, although it is attenuated by free-free absorption at the lowest frequencies. The observed spectrum of synchrotron emission can be described by the power-law $S_\nu \propto \nu^{-0.8}$ (see Fig. 2.1). The power-law index depends on the distribution of energy of the ensemble of emitting particles (relativistic electrons). Since the particles lose energy, they will eventually stop emitting radio emission if new energy (or new particles) is not injected.

The inverse process is also possible, i.e. that a charged particle in a magnetic field absorbs a photon. This is called synchrotron absorption, but is a minor effect except in extremely bright ($T_b \sim 10^{10}$ K; Condon (1992)) objects.

2.2 The evolution of radio supernovae

Massive $M > 8M_\odot$ stars may end their lives as core-collapse supernovae (SNe). In these spectacular events, the stellar core collapses inwards and ends up as a very dense and compact object, a neutron star or a black hole. The outer layers are ejected as a shock wave traveling outwards with speeds $> 10000\,\mathrm{km/s}$ (Chevalier 1982; Chevalier 2007). During the explosion a huge amount of energy is released, typically 10^{51} ergs. When the ejecta interacts with the circumstellar medium (CSM), a part of this energy (typically 2%; Lacki et al. (2010)) goes into ultra relativistic electrons which interact with strong magnetic fields in the shock wave to produce synchrotron radiation. Before the explosion, stellar winds may push away circumstellar matter from the regions close to the star, creating a ”wind-blown bubble” with a radial density profile $\rho \propto r^{-2}$. Therefore, there is a delay from the actual explosion until the maximum amount of synchrotron emission is produced.

The time when the ejecta has swept up a mass of circumstellar material equal to the mass of the ejecta itself is usually called the Sedov time. At this stage, a reverse shock is formed traveling inwards, and the radio emission from the

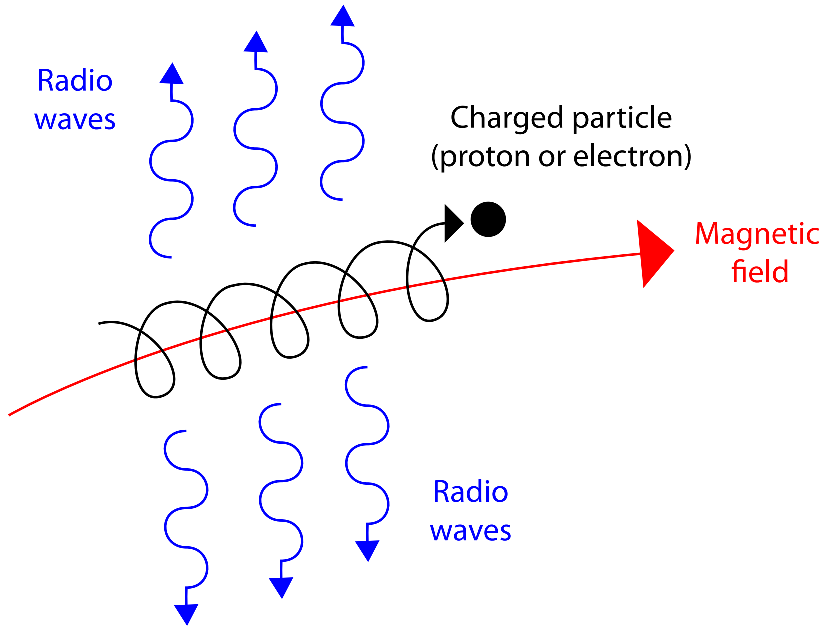

Figure 2.2: Charged particles spinning around magnetic field lines produce synchrotron radiation. Detecting synchrotron radiation from space at radio wavelengths allow us to study astrophysical phenomena such as supernovae in detail. Image credit: High-res. version by Simon Farsi, original at http://nrumiano.free.fr/PagesU/Elexique.html.

shocked CSM starts to slowly decline. The supernova has now evolved sufficiently for us to refer to it as a *supernova remnant* (SNR). The evolution of the observed brightness at a specific wavelength as a function of time is called the *light curve*. Because of the dependence of the light curve on the shape and density of the circumstellar material, radio observations can be used to constrain the mass-loss history of the progenitor star, i.e. before it exploded as a supernova remnant. Also, SNe and SNR can be used as in-situ probes of the densities in the CSM, and of magnetic fields present in the supernova shocks. This gives us valuable detailed information about the physics in regions of star formation.

2.3 The FIR/radio correlation

There is a strong observed relation between the luminosity of a galaxy at radio and at infrared wavelengths, and this is usually called the FIR/radio correlation. The tight relation between the two wavebands is usually explained by star formation as the source of emission in both wavebands. The infrared emission is thought to be thermal re-radiation from dusty HII regions; the UV-light from stars is absorbed by dust and converted to infrared. The radio emission is thought to be dominated by synchrotron radiation from relativistic electrons accelerated in supernova remnants. It has been proposed that the FIR/radio correlation can be used to separate star forming galaxies from active galaxies (AGNs, hosts of highly-accreting super-massive black holes), but it is also interesting in itself because of the tight connection to the physics of star formation.

The correlation is usually described in terms of a logarithmic ratio , q, between flux densities at FIR and radio wavelengths:

$$q \equiv \log\left(\frac{\mathrm{FIR}}{3.75\times 10^{12}\mathrm{Wm}^{-2}}\right) - \log\left(\frac{S_{1.4\mathrm{GHz}}}{\mathrm{Wm}^{-2}\mathrm{Hz}^{-1}}\right) \tag{2.1}$$

where $S_{1.4\mathrm{GHz}}$ is the observed 1.4 GHz flux density in units of $\mathrm{Wm}^{-2}\mathrm{Hz}^{-1}$ and

$$\mathrm{FIR} \equiv 1.26\times 10^{-14}(2.58 S_{60\mu m} + S_{100\mu m}) \tag{2.2}$$

where $S_{60\mu m}$ and $S_{100\mu m}$ are the IRAS 60 and 100 μm band flux densities in Jy (Condon 1992). A large value of q means little radio emission in relation to FIR. The relation is remarkably tight over several orders of magnitude in luminosity. Very few galaxies differ more than a factor of 5 from the average value $q = 2.34$, see Fig. 2.3. One such unusual galaxy is NGC 4418, discussed in Sect. 6.

2.3.1 A more elaborate model of the FIR/radio correlation

The wide range of properties of galaxies following the FIR/radio correlation has inspired studies trying to explain the physics behind this relation in detail. The simple calorimeter model, meaning that all UV light is re-radiated as infra-red and all electrons radiate their energy as synchrotron emission, is probably not true. Lacki et al. (2010) argue that since most normal galaxies show a significant UV luminosity, not all can be absorbed by dust. Also, if the electrons lost all their energy before leaving the galaxy the spectral index α would be around -1, but instead it is ~ -0.8 as mentioned above. Therefore, a significant fraction of charged particles must leave normal galaxies before radiating all their energy.

Lacki et al. (2010) present a more detailed model trying to explain the physics of the FIR/radio correlation. The basic radio source is still the relativistic electrons, called primary electrons. But, in dense starbursts the production of high-energy cosmic rays (CR; high energy protons and atomic nuclei) are also important. Collisions between CR protons and protons in the interstellar medium (ISM) produce pions, which decay into gamma rays, neutrinos and *secondary* electrons and positrons. Lacki et al. (2010) found that secondary electrons and positrons likely are comparable to, or dominate, primary electrons in dense starbursts. However, the increased number of relativistic particles that could

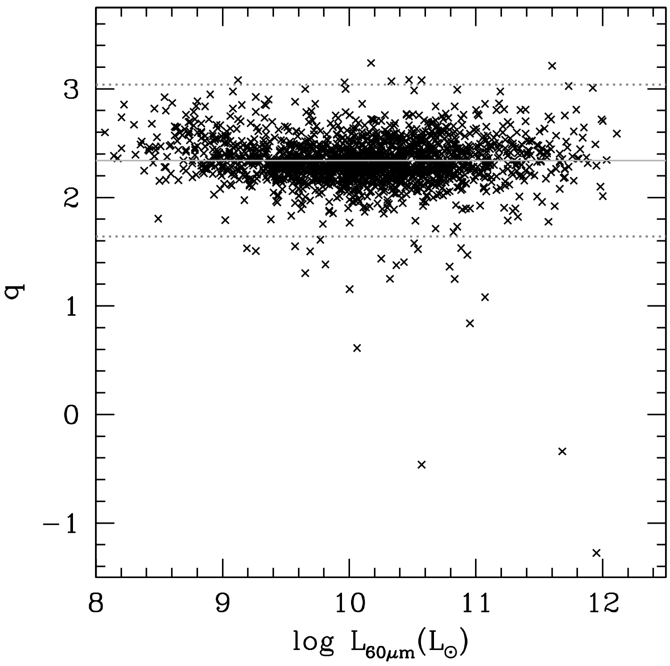

Figure 2.3: Distribution of q-values plotted as a function of IRAS 60 μm luminosity, from Yun et al. (2001). The solid line marks the average value of $q = 2.34$, while the dotted lines delineate the "radio-excess" *(below)* and "IR-excess" *(above)* objects, delineated for having 5 times larger radio and IR flux density than the expected values from the linear radio-FIR relation, respectively.

produce more synchrotron radiation is mitigated by inverse Compton scattering and ionization losses. Together, these two effects cancel out to result in the FIR/radio correlation for dense starbursts.

For low surface density galaxies, Lacki et al. (2010) found that the charged particles escape the galaxy before loosing all their energy, hence they would appear weaker in the radio. However, these galaxies are also less dusty, thereby decreasing the UV-opacity which decreases the FIR luminosity. Once again, the effects conspire to produce the correlation also for low density environments.

To test models of the FIR/radio correlation, such as presented by Lacki et al. (2010), we need to study galaxies with different properties at many different frequencies. Two galaxies following the correlation are M82 (which is a nearby well studied star forming galaxy) and Arp220 (which is bigger, more luminous and further away). Important clues about the physics might also be found from studying the few galaxies not following the correlation, such as the galaxy NGC 4418.

Chapter 3

Interferometry

This thesis rests on interferometry as an observational technique. The knowledge of interferometry is vast and is challenging to convey in a brief and clear way. Since there are many excellent textbooks available on the subject, for example Thompson et al. (2001) and Taylor et al. (1999), I will not try to redo their explanations in this thesis. However, during my work I have found it useful to collect in one place my own understanding of how to estimate coherence losses due to averaging of interferometric data.

3.1 The small field-of-view approximation

When the field of view is small the relation between the measured visibility $V(u,v)$, the image $I(l,m)$ and the antenna reception pattern $A(l,m)$ can be written as the familiar Fourier transform

$$V(u,v) = \int_{-\infty}^{\infty}\int_{-\infty}^{\infty} A(l,m)I(l,m)e^{-2\pi i(ul+vm)} \tag{3.1}$$

where l,m are the sines of the angular separations of the pixels in the image with respect to the phase center (see Taylor et al. (1999), Chap. 2: Fundamentals of Radio Interferometry). The parameters u and v are the projected east-west and north-south components of antenna baselines measured in wavelengths, defining a *uv-plane* also referred to as *Fourier space*. The *visibilities* $V(u,v)$ are samples of the Fourier transform of the image. Remembering that for small angles $sin(\theta) \approx \theta$ we see that a point source (Dirac delta function) in the image at angular distance l radians from the phase center will transform to a plane wave in Fourier space with wavelength $1/l$. The larger offset l in the image, the shorter wavelength in Fourier space. Because of rotational invariance of the Fourier transform, the plane wave will have the same direction as a vector pointing from the phase center to the displaced point source in the image.

3.2 Averaging of plane waves in Fourier space

Since correlators output a discrete set of visibilities (i.e. samples in time and frequency), averaging is to some extent always done on interferometric data. We may also average the data further after correlation to reduce the computational resources needed for calibration and imaging. Any averaging must however be done with care. Averaging a range of samples in time and frequency together corresponds to averaging over a small parallelogram in Fourier space. This means some information is lost, and one has to take care to not lose information that could affect the scientific results.

One way to estimate the effects of averaging is to imagine we have a single point source in our image. If this source is at the phase tracking center, $(l, m) = (0, 0)$, it is not affected by averaging. If however the source is at some offset from the phase center, then its Fourier transform will be a plane wave. If averaging in Fourier space while there is a plane wave present, the amplitude of the plane wave will be reduced. This is called coherence loss.

A linear slice in any direction through Fourier space containing a plane wave can be described as a sequence of complex numbers. If we assume a linear phase dependence within this sequence (i.e. an ideal wave) we can represent the sequence of numbers as phasors. When averaging along any direction, for example in frequency, the maximum coherence loss will occur if we average in the direction of the plane wave. In the following derivation, we assume maximum coherence loss to estimate the maximum possible effect on the final images.

If we average over a length Δu in Fourier space, we will average all phasors within this length. The phasor angles of the plane wave will cover uniformly an angle of $\Delta\phi = 2\pi l \Delta u$ (i.e. the fraction of a full period of the plane wave). Since we are only interested in the fractional loss, we can without loss of generality represent the phasors as a set of unit vectors with angles in the range $\pm\Delta\phi/2$, see Fig. 3.1.

If we average these vectors together, we get one single vector with the average phase 0 (because of our chosen reference) and an amplitude being the normalized sum of all projected amplitudes. The resulting average amplitude a can now be written as

$$a = \frac{\int_{-\Delta\phi/2}^{\Delta\phi/2} \cos(\theta) d\theta}{\int_{-\Delta\phi/2}^{\Delta\phi/2} d\theta} = \frac{\sin(\Delta\phi/2)}{\Delta\phi/2} \tag{3.2}$$

where θ is the phasor angle and cosine is the projection effect when averaging unit vectors. If we define the coherence loss L as the reduction in amplitude, we get $L = 1 - a$. For small changes in phase we can approximate this with the first two terms in the Taylor series for the sine function:

$$L \approx \frac{(\Delta\phi/2)^2}{3!} = \frac{(\pi l \Delta u)^2}{6}. \tag{3.3}$$

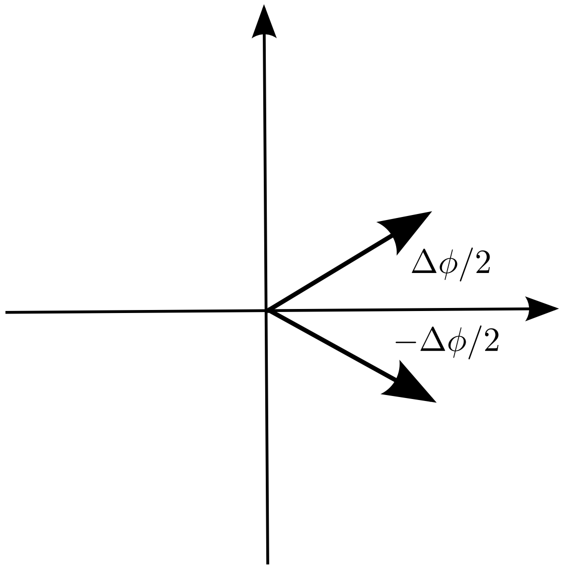

Figure 3.1: We can without loss of generality represent the phasors as a set of unit vectors with angles in the range $\pm\Delta\phi/2$, i.e. as all vectors with angles between the two shown in this figure.

Hence, the coherence loss depends on the path length Δu that we are averaging in Fourier space, as well as on the offset l in the image. The loss is more severe for sources far away from the phase center.

3.2.1 Coherence loss due to time and frequency averaging

Coherence loss due to time and frequency averaging is also referred to as time and bandwidth *smearing*, illustrated in Fig. 3.2 The following text will be approximate to derive an upper bound, i.e. worst case loss. For a more elaborate description, see Taylor et al. (1999), Chap. 18: Bandwidth and Time-Average Smearing.

Time smearing

If we average during a time Δt, the path length in Fourier space is the arc followed by the motion of the (projected) baseline relative to the sky during Δt. To a good approximation, the path length can be described as the arc due to the Earth's rotation. This path is normally not a straight line, but to get an upper bound (i.e. worst case) we assume a path length equal to the arc. Also, we assume for simplicity that we are imaging the North celestial pole, where the motion will be most severe. In this case, for baseline of length u (in units of observing wavelengths), the path length $\Delta u = u\Delta t\omega$ were ω is the angular rotation

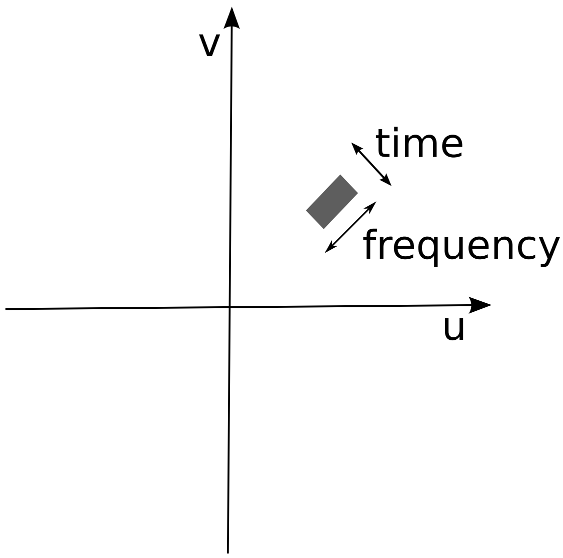

Figure 3.2: Schematic view of averaging in time and frequency in Fourier space. The radial direction corresponds to frequency, and our calculation of coherence loss due to frequency averaging is exact. The angular direction corresponds to time, and depends on the orientation of the specific baseline with respect to the source. For this effect we estimate the worst case, i.e. an upper bound of the loss.

of the Earth around its axis (i.e. approximately $2\pi/$(23h56m)). Using this path length in eq. 3.3 we see that the loss due to time averaging is worse for longer baselines.

Example: The longest international LOFAR baseline used in the observations of M82 in Chap. 5 is 1158 km (van Haarlem et al. 2013). Let us assume we observe at frequency 154 MHz and have a source 30″ from the phase center. If we average 10s, the coherence loss will be less than 0.65%. This is negligible, so if this is our desired field of view there is no need to worry. There might however be other effects to worry about such as primary beam effects, or residual rates and delays in the data (see below).

Bandwidth smearing

If averaging over a frequency range $\Delta\nu$ for a baseline u (in units of observing wavelength), we are summing phasors along a path $\Delta u = u\Delta\nu/\nu$ where ν is the observing frequency, i.e. the fractional bandwidth times the baseline length. Example: Again LOFAR, but now we average in frequency to 1 channel per LOFAR subband, i.e. a frequency resolution of 195 kHz. For the longest international baseline of 1158km, and a source at 30″ from the phase center, we estimate 1.98% coherence loss due to frequency averaging. Note that in contrast to time averaging where we get an upper limit, the calculation of frequency averaging is exact because the path Δu is always in the radial direction in Fourier space.

3.2.2 Effect on size measurements

A loss of amplitude is easy to see as a loss of signal. However, since the effect is dependent on baseline length, averaging might also affect the structure we see in the image. Because the amplitude drops the most on the longest baselines (highest spatial frequencies), too much averaging will result in objects looking bigger than they really are. This will be seen in the image as an increase in source size as a function of distance to the phase center. This is dangerous because this effect could be interpreted as a real trend in sizes. Therefore it is very important to check the impact of averaging on each dataset.

3.2.3 Coherence loss due to residual delays and rates

In interferometric data, especially VLBI, there might be residual delays and rates left after correlation. This is because the correlator model is not good enough to completely account for all small errors introduced, mainly by clock drifts and ionospheric disturbances. Residual delays for one antenna means that all baselines related to that antenna have the phase center slightly offset with respect to the desired position. The offset l_τ in radians due to a delay error τ can be calculated as

$$l_\tau = \arcsin(\tau\nu/u) \tag{3.4}$$

where u is baseline length (in units of observing wavelength) and ν observing frequency, see Chap. 2 in Taylor et al. (1999). A 300 ns delay error when observing with the longest LOFAR baseline at 154 MHz is equivalent to using an offset of $l = 16''$in eq. 3.3, i.e. a smearing loss due to 195kHz frequency averaging of 0.56% and due to 10s time averaging of $< 0.19\%$.

Residual rates will cause the true visibility phases to change within the averaging time or frequency interval, even if the source is at the phase center. A residual rate of r mHz (cycles per second) will result in a change of phase within ts of $\Delta\phi = r \cdot 10^{-3} \cdot 2\pi \cdot t$ radians. Example: A residual rate of 3 mHz when averaging over 10s will result in a change of phase of 10.8°. This is acceptable, but if rate corrections are derived and corrected for in the Astronomical Image Processing System (AIPS, Greisen (2003)), the calibration routines will correct losses in amplitude due to the known residual rates (see Fig. 22-2, Chapter 22: Very Long Baseline Interferometry, Taylor et al. (1999)) . Since we use AIPS to derive and apply residual rate corrections for our M82 LOFAR data in Chap. 5 we need not worry about the amplitude loss due to the typical rates of 3 mHz found in the data.

Chapter 4

Studying supernovae in an extreme environment: Monitoring of Arp 220

Arp 220 is an ultra luminous infrared galaxy (ULIRG) at distance 77 Mpc. It is in fact two galaxies in the process of merging, even though it is hard to see the two nuclei in Fig. 1.4(a). The two nuclei are called the East and West respectively, and are separated by an angular distance of about 1″ on the sky. Analyzing single objects within these nuclei obviously requires very high-resolution imaging. Because of the high dust obscuration, radio VLBI is the optimal way to get high-resolution information of what is happening in the two nuclei. Studying Arp 220 gives us a lot of information about the physics of star formation. In particular, we increase our knowledge of star formation in merging galaxies. Merger driven star formation is thought to be much more common in the earlier Universe than today, and therefore studies of Arp 220 may contribute with a small piece of the puzzle of galaxy evolution.

The existence of several discrete compact radio sources in Arp 220 was first reported by Smith et al. (1998). Our group has a long history of monitoring and analyzing the compact sources in Arp 220 with the most recent study published by Batejat et al. (2011). Monitoring has continued, and we have several new data sets to help us understand what is going on in detail in the two nuclei of Arp 220.

4.1 Scripted calibration and imaging of VLBI data

The fact that regular monitoring of Arp 220 has been going on for over a decade means there are a lot of data available. These data have been calibrated, imaged and published by different people using slightly different software and techniques. In general, VLBI results are robust enough to be trustable within the

Table 4.1: List of calibrated and imaged VLBI data sets on Arp 220. Note: the rms noise levels for epochs GC031A, B, and C are given after correcting for the systematic offset in amplitude as described in appendix A.1. Also note that BB297B and BB297C are ongoing work.

Epoch	Obs. date	Wavelength [cm]	Beam size [mas]	Image noise [μJy/beam]
GD017A	2003-11-09	18	6.84×2.67	12
BP129	2006-01-09	6	2.64×1.37	52
GC028A	2006-11-28	3.6	1.32×0.52	37
GC028B	2006-12-28	0.7	1.10×0.32	29
GC031A	2008-06-10	6	2.21×0.76	13
GC031B	2008-10-24	6	1.90×0.81	10
GC031C	2009-02-27	6	2.04×0.79	12
BB297A	2011-05-16	6	1.97×1.01	13
BB297A	2011-05-16	3.6	1.10×0.49	21
BB297A	2011-05-16	18	9.92×3.65	35
BB297B	2011-05-16	6, 3.6	N/A	N/A
BB297C	2011-05-16	18, 6, 3.6	N/A	N/A

errors given, even if derived by different people, but since we are looking for long-term trends in the data also for the weaker sources, we would like to have data calibrated and imaged as homogeneously as possible.

Previously, most calibration and imaging has been carried out by hand using the Astronomical Imaging and Processing Software (AIPS, Greisen (2003)). This is time-consuming, but the process can be speeded up considerably by using a wrapper code in Python to enable scripting: a software called ParselTongue, developed by Kettenis et al. (2006). Using this software I have re-calibrated from scratch several VLBI data sets from observations of Arp 220, see Table 4.1. The calibration was done in a semi-automated manner, where the results of each calibration step was inspected by hand in AIPS, but the knowledge from calibration of one dataset was quickly transferable to other data sets by minor changes in the Python scripts.

Using ParselTongue, we also developed an automatic way of imaging all the calibrated data sets with the same imaging parameters (cell size, weighting etc.) The imaging works by using the Autoboxing feature in the AIPS task CLEAN, together with a list of known source positions (from earlier epochs). In the first of three stages, boxes are placed on emission stronger than 5.67σ (corresponding to a probability of false detection of 0.2% in a 8192×8192 pixel image). After cleaning the strongest sources, the second stage begins where boxes are placed if there is emission with a peak above 3.96σ at a position previously known as a source (i.e. using the Bayesian approach of including prior information). In the third and final stage, deconvolution is allowed to pick freely the remaining peaks of emission from the residuals. The beam size and noise rms of the processed images are given in Table 4.1.

While comparing light curves for all sources we found a systematic offset of too high amplitudes in the three epochs GC031A, B, and C. This difference was concluded to be due to some error in the correlation process and we re-scaled the amplitudes of these epochs to match the linear decline expected for several long-lived sources. For more details on this discrepancy, see appendix A.1.

Some epochs have been imaged and published before, and the new results are generally in good agreement. Some epochs have not been published before, for example BB297A used to illustrate this chapter. Using data from all epochs together, we aim to describe in detail the properties and recent evolution of the compact sources detected in Arp 220. This is currently work in progress, but I will briefly present below a few preliminary results.

4.2 Preliminary results

An image of the western nucleus, made from data observed in project BB297A at 6 cm, is shown in Fig. 4.1. Combining the data from four 5 GHz epochs,

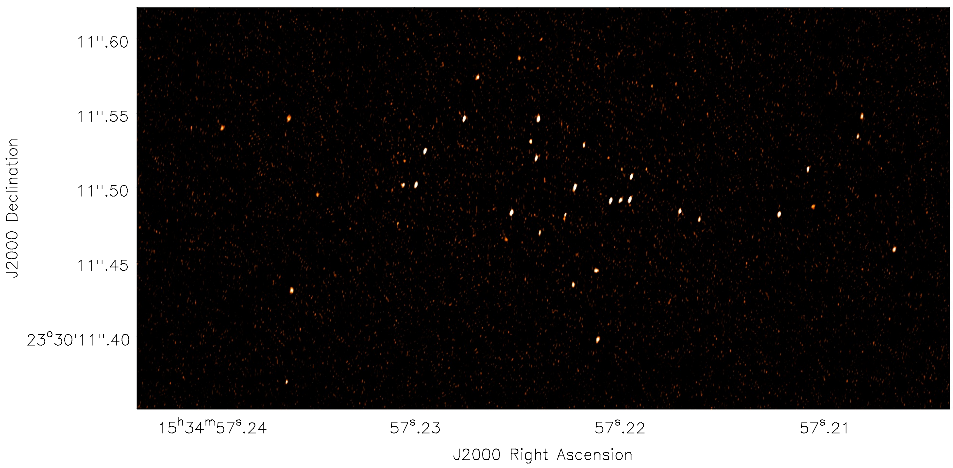

Figure 4.1: The western nucleus of Arp 220 as imaged using the calibration and imaging explained in Sect. 4.1. The image RMS noise is 13μJy/beam and the resolution is 1.97 mas$\times$1.01 mas. More than 40 discrete objects are brighter than our detection threshold of 5σ. This image was made from data taken on May 16, 2011 as part of project BB297A, see Table 4.1. A manuscript with detailed analysis of this and other images of Arp 220 from the data presented in Table 4.1 is in preparation by Batejat et. al 2014.

GC031A,B,C and BB297A, we have measured the average size and luminosity of all detected sources. Plotting luminosity vs size we obtain the classical Power-Diameter diagram, see Fig. 4.2. Using all the data (light curves and spectra) we have classified all sources into eight categories, and the sources are marked accordingly in Fig. 4.2. All details of the classification will be published by Batjeat et al 2014, currently in preparation. The objects E10 in the eastern nucleus and W55 in the western nucleus show an inverted spectra, and both are centered in their respective nuclei. We believe these could be AGN candidates of the two nuclei, but this needs to be further investigated before it is confirmed. The green sources are transition objects, which we believe are on their way to becoming supernova remnants. The red objects are remnants, with larger sizes and fading light curves.

It is clear from Fig. 4.2 that there are many weak, small objects. If all of these were supernovae, we would expect many more large remnants than we see. We instead proposed the hypothesis that a large fraction of these objects are in fact old remnants, where we only see a small part of the large but weak shell. Since we are limited by noise, we would not see all the weak and big remnants which must be there to continue the evolution after the largest sizes we measure. To investigate this we performed Monte Carlo simulations of supernova evolution to see if we could reproduce Fig. 4.2 with large but weak remnants as a part of the many weak sources detected.

4.2.1 Modelling the PD-diagram as supernova evolution

Preliminary results suggest that we can reproduce Fig. 4.2 by modelling of supernovae evolving in a circumstellar medium of density $n_H \approx 0.8 \cdot 10^4$cm^{-3}. Here we assume an ejecta mass of $1M_{\odot}$, an explosion energy of $2.8 \cdot 10^{51}$ergs, and a supernova rate of 0.25/yr. We define the expansion velocity as in Draine et al. (1991) and the initial flux density of new SNe is extrapolated from Berezhko et al. (2004) to our dense environment. The supernova rate is lower than previous estimates for Arp 220 (4±2/yr; Lonsdale et al. (2006)), and I want to stress that these results are preliminary. However, our modelling shows that it is possible to explain the number of sources and the shape of Fig. 4.2. In particular we were interested in the large number of very faint sources. Our simulations are consistent with a part of these being SNe, but a large fraction is probably large weak remnants where we only detect the brightest part of the expanding shell. This is also consistent with our detection limit.

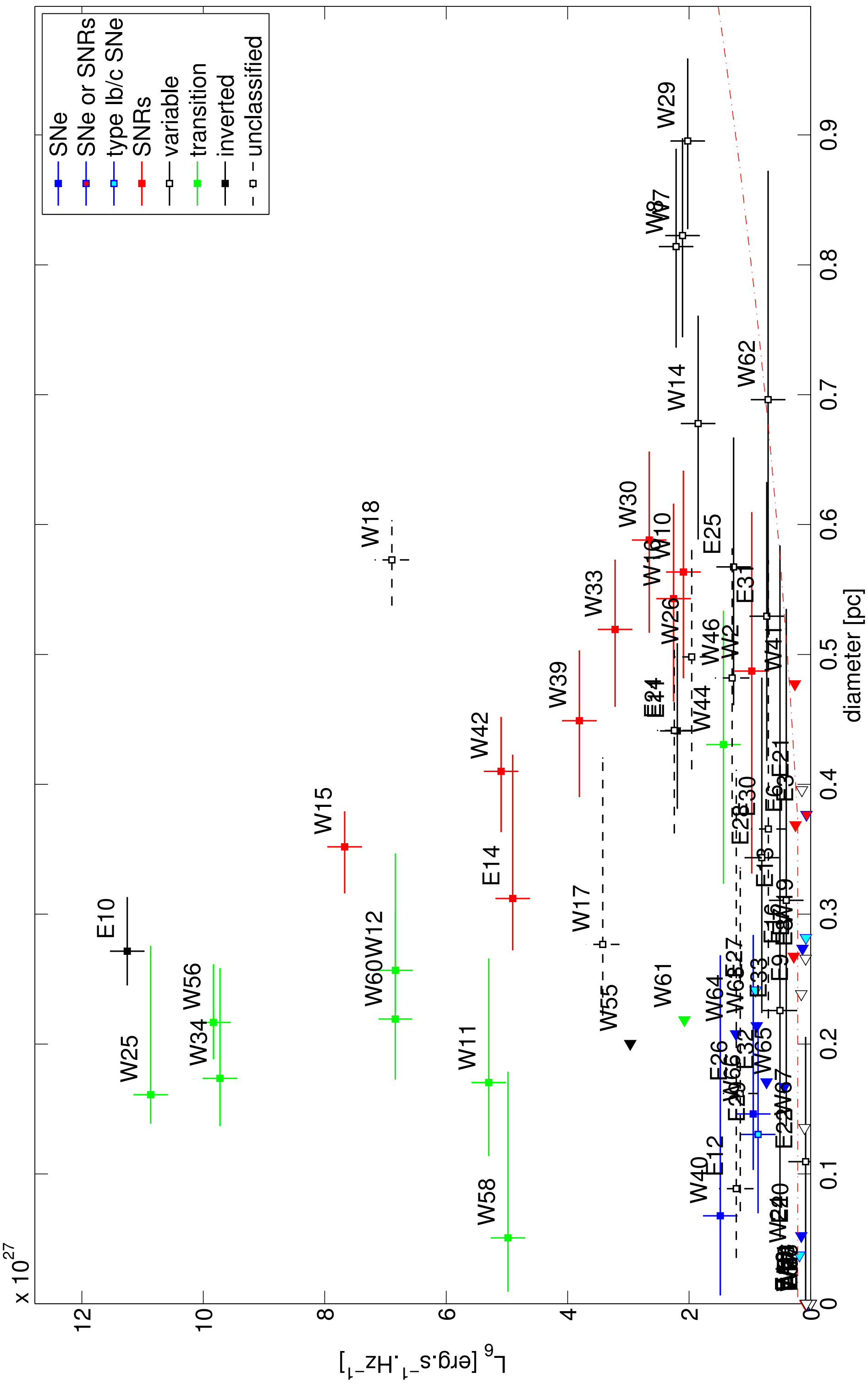

Figure 4.2: Power-Diameter diagram for the compact sources in Arp 220. The data are from four combined 5 GHz observations: epochs GC031A,B,C and BB297A. The sources were classified according to their light curves and spectra (ignoring their position in this plot). Sources from the same class are close in this plot, indicating that our classification is sensible. The dashed red line is the detection limit: for sizes smaller than the beam, the limit is 3σ, for sizes greater than the largest beam the detection threshold is $3\sigma \cdot (\text{diameter}/\text{beam})^2$. Figure from (Batejat et. al 2014, in preparation). The beam used is the largest, and σ the smallest of the four.

4.3 Future work

The preliminary results of the monitoring data are promising and we aim to publish a first part of the analysis in the near future. In addition to the current data, we have been granted in total 24 hours of new observations at 3.6 cm, 6 cm, and 18 cm of Arp 220 with the high sensitivity array (HSA) in the USA. We hope these observations (project BB335) will be carried out as planned during summer 2014, and we aim to image and analyze these new results before the end of this year.

Chapter 5

A new record in resolution at low frequencies: M82 with LOFAR

M82 is a nearby (3.6 Mpc) starburst galaxy which has been the subject of numerous studies. The close distance makes it easier to study compact objects thought to be SNe/SNRs in detail, using for example the eMERLIN interferometer. The long term monitoring available since 1981 has resulted in detailed knowledge of the evolution of 52 compact objects, mostly identified as SNe/SNRs and HII-regions (Gendre et al. 2013). There is also a strong diffuse component surrounding the compact sources, visible for example in the natural weighted image of Wills et al. (1997).

To spatially trace the free-free absorption, high-resolution images are needed at low frequencies. However, no images with high enough resolution have been available for frequencies below 300 MHz. Using the international LOFAR telescope (including our station in Onsala), we have made for the first time a sub-arcsecond resolution image of M82 at 154 MHz.

5.1 Calibration

Since the calibration procedure we used for these data has not been used before, I want to briefly summarize the steps taken here. For those interested in details, I also include a detailed description of the calibration in appendix A.3.

Because of the large data volumes of a few TB, the data were first averaged to to 1 ch/subband and 10s integration time. We estimate the effects of smearing to be small up to 30″from the phase center (see also examples in Chapter 3). Because of the need to derive delay and rate corrections using AIPS (Greisen 2003) the data were converted from linear to circular polarization. The calibration was then carried out within AIPS. The strong (90 Jy) source 3C196 was used as flux density calibrator. The source J0958+6533 (known to be 0.74 Jy at 74 MHz in VLSS) was observed to estimate delay, rate and phase corrections at an angular distance of 3.5°from M81. The corrections were transferred to M81 (0.61°from M82), and the phase calibration was refined using a point source model. The calibration was applied to M82, and after phase-only self-calibration the cumulative corrections were applied to M82 and the data exported to CASA 3.4 (McMullin et al. 2007) for imaging.

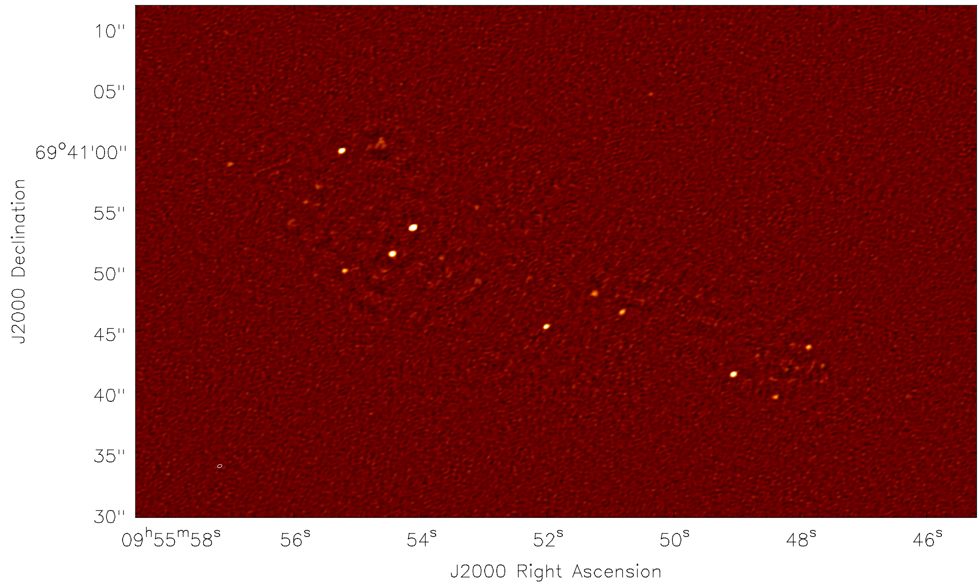

Figure 5.1: Image of M82 at 154 MHz using LOFAR baselines longer than $75\,\mathrm{k}\lambda$. The image RMS noise is 0.17 mJy/beam. The beam of 0.387″×0.242″ is shown in the bottom left. The total integrated flux of the compact components detected over 5σ is 77 mJy. Including also flux density present in features above 3σ but below 5σ, the total flux density in this image is ~ 100 mJy. (Varenius et al. 2014, in preparation).

5.2 Preliminary scientific interpretation

Our image of M82 (see Fig. 5.1) is a new world record in terms of resolution at low frequencies. This image was made using only the longest LOFAR baselines $> 75\,\mathrm{k}\lambda$. In addition, we also have data for the shorter LOFAR baselines, and using baselines of length between $2\,\mathrm{k}\lambda$ and $75\,\mathrm{k}\lambda$ we produced a lower resolution image, see Fig. 5.2. This image seems to show the effects of outflow above and below the edge-on star-forming disk, together with strong free-free absorption in the plane of the disk where most SNRs are located.

The compact objects visible in Fig. 5.1, are all known from other observations at higher frequencies. We are currently analyzing and comparing the new data to previously published values constrain their radio spectra. We do not have final results yet, but I will discuss a few preliminary results below.

5.2.1 SN2008iz

The first bright radio supernova ever to be observed in the starburst galaxy M82 exploded in 2008; being detected serendipitously in VLA 22 GHz observations made for another purpose (Brunthaler et al. 2009). Based on unpublished multiple frequency monitoring, a mini-shell model was fitted to predict a flux density of 140 mJy in January 2013 at 150 MHz. Our observations were delayed until March, but we would still expect to see a clear signal from SN2008iz. However, looking at position R.A. $09^h55^m51^s.5500$, Dec. 69°40′45″.792 (as given by Brunthaler et al. (2009)) the peak is only 0.32 mJy/beam i.e. less than 3σ. This upper limit may revise the evolutionary models of this supernova or, perhaps more likely, suggest the presence of strong free-free absorption in the foreground of SN2008iz.

5.2.2 The brightest object detected at 154 MHz

The peak of 16.8 mJy/beam in Fig. 5.1 is located at position R.A. $09^h55^m54^s.13$ and Dec. 69°40′53″.6 (J2000), which coincide very well with the source called 45.42+67.4 by Gendre et al. (2013). This object was listed by with a peak flux density of 0.28 mJy/beam and integrated flux density of 2.56 mJy at 5.0 GHz. We measure an integrated flux associated with this source of 19.21 mJy at 150 MHz, implying a spectral index $\alpha = -0.57$ between 5 GHz and 154 MHz, where $S_\nu \propto \nu^\alpha$. This is in good agreement with -0.6 derived by Wills et al. (1997) for this source at 408 MHz and is a bit surprising. We would have expected a low-frequency turn-over due to free-free absorption to make this source fainter at 154 MHz. Perhaps the free-free absorption is clumpy as suggested by Lacki (2013), or perhaps this source is located on the near side of the galaxy with respect to us (and SN2008iz at the far side).

5.3 Future work

In the near future, we hope to publish the high-resolution images obtained of M82 in a scientific journal. We are currently analyzing the data in more detail to arrive at a more complete scientific interpretation than the preliminary results presented above.

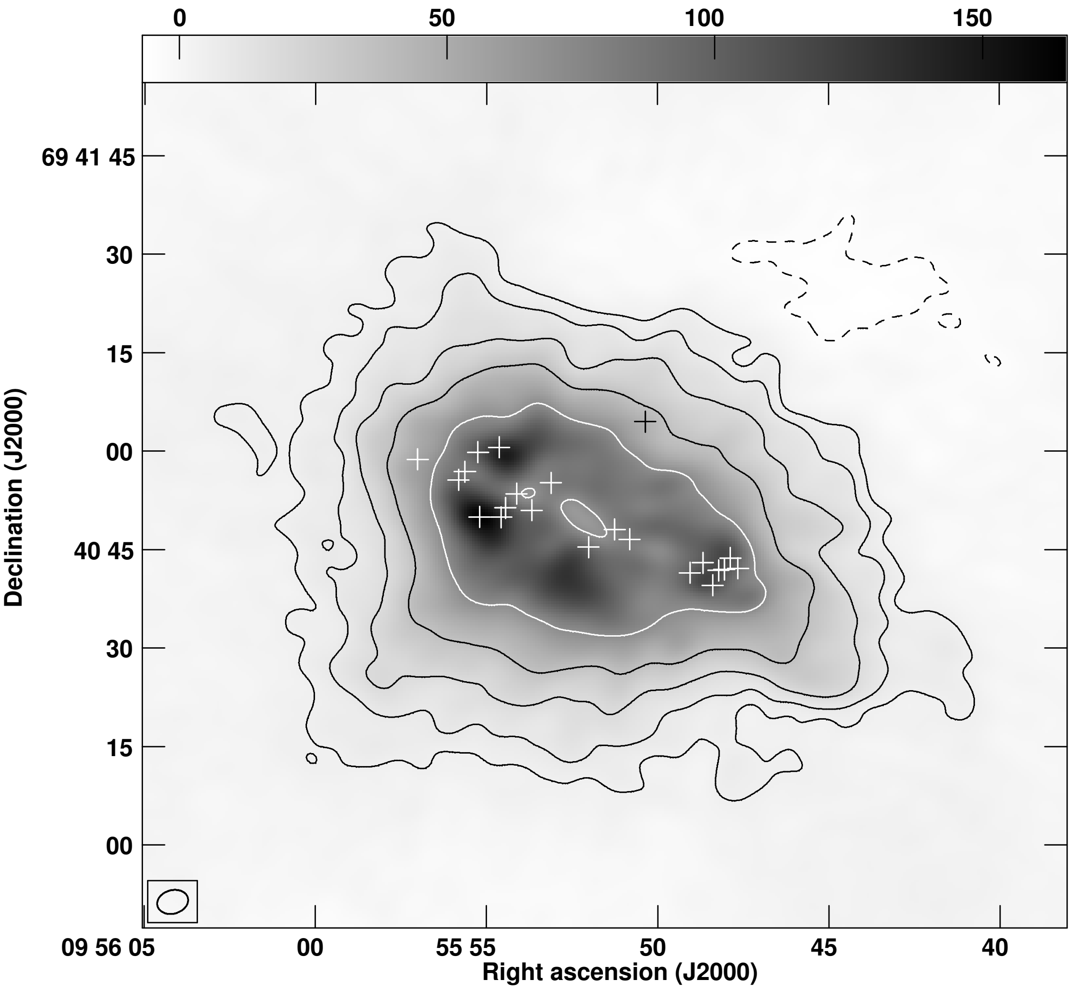

Figure 5.2: Image of M82 at 154 MHz using LOFAR baselines of length between 2 kλ and 75 kλ. The image was deconvolved using robust 0 weighting and the RMS noise is 0.44 mJy/beam, with contours at (-10, 10, 20, 40, 80, and 160) times the noise. The beam of 4.79″×3.57″ is shown in the bottom left as a filled ellipse. The plus signs mark the positions of the 22 compact sources detected above 5σ mJy/beam in Fig. 5.1. The grey scale is in units of mJy/beam. (Varenius et al. 2014, in preparation).

Chapter 6

Introduction to paper I: What is powering NGC 4418?

The galaxy NGC 4418 is very bright in infrared but very dim in radio, compared to what we expect from the standard FIR-ratio correlation (see Sect. 2.3, q=3.075; Yun et al. (2001)). The high infrared luminosity of more than $10^{11} L_\odot$ means this galaxy qualifies to be classified as a *luminous infrared galaxy* (LIRG). Where does this enormous amount of infrared light come from? Two main scenarios have been proposed. Either the galaxy hosts a radio-weak active galactic nucleus (AGN) or, it hosts a very young and compact starburst. A mix between the two is also possible (Roche et al. 1986).

Unfortunately, NGC 4418 is extremely obscured by dust and it is therefore very hard to study the nucleus at optical wavelengths. Optical spectroscopy could otherwise prove the existence of a young starburst by for example detecting spectral signatures of young massive Wolf-Rayet (WR) stars, as described by Armus et al. (1988). The H_2 column density is so high ($> 10^{25}$cm^{-2}; González-Alfonso et al. (2012)) that the nucleus is *Compton thick* so that X-ray measurements are also inconclusive (Maiolino et al. 2003). It is however possible to see through the obscuring material at radio wavelengths. From previous studies, we know that the central IR power source has a small angular size of less than 0.1″(Sakamoto et al. 2013, or 20 pc at distance 34 Mpc). Therefore, to make sharp enough images of NGC 4418 at cm wavelengths we need to use very long baseline interferometry.

This galaxy had been observed as a joint EVN and MERLIN project in 2001. The MERLIN part had been published by Costagliola et al. (2013) but the EVN part had not yet been imaged. We calibrated the EVN data and made a combined image of the very center of NGC 4418 (see Fig. 6.1, also as Fig. 2 in Paper I) using both EVN and MERLIN.

This image for the first time reveals a complex structure in the form of eight

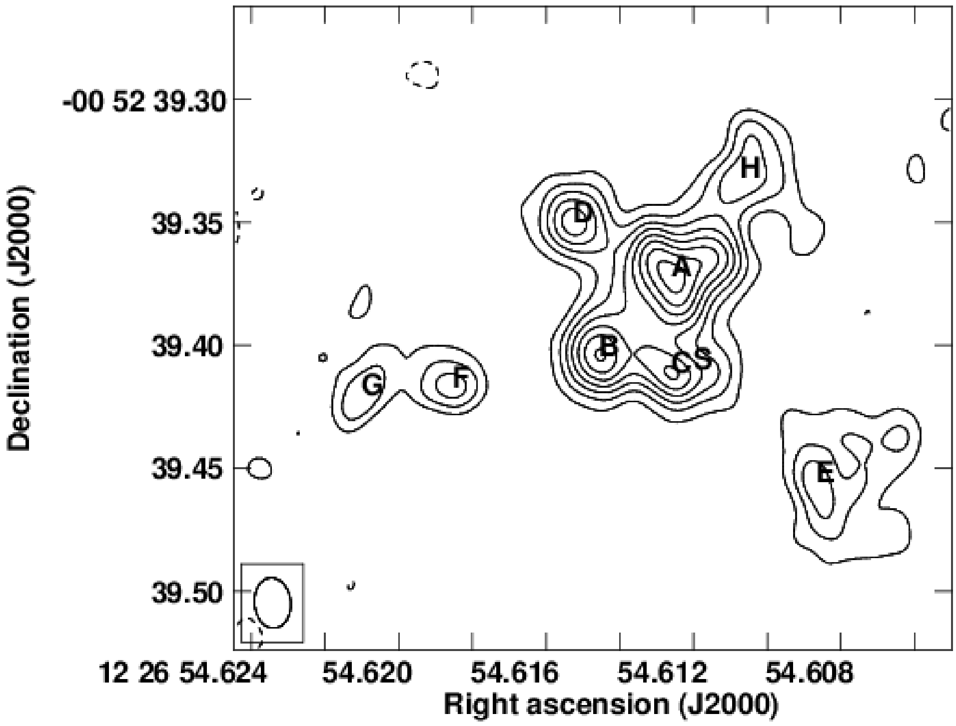

Figure 6.1: EVN+MERLIN 5 GHz image of NGC 4418 with relative weight 1.0 between the MERLIN and EVN data. The contour levels are (-2,2,4,6,8,10,12,14,16) times the RMS noise of $\sigma = 90\mu$ Jy/beam. Eight compact features are visible above 5σ labelled from A to H. The label S (close to label C) corresponds to the 860 μm continuum peak position from Sakamoto et al. (2013). The CLEAN restoring PSF of FWHM 20.6 mas$\times$14.8 mas is plotted in the lower left.

compact components. The complicated structure detected is a strong argument against ONLY an AGN; there must also be a significant contribution from star formation to create this non-linear structure. We believe that the compact features we see are evidence for intense star formation in the form of massive $10^7 M_\odot$ super star clusters (SSCs).

Sakamoto et al. (2013) estimates that any star formation component must be younger than 30 Myr to explain the faint radio emission. However, we expect even a young starburst to have a steep spectrum typical for synchrotron emission from supernovae ($S_\nu \propto \nu^{-0.8}$, see Sect. 2.1.2). But, when we compare the flux densities measured in compact structure at 1.4 GHz and 5 GHz we see the opposite: more emission at 5 GHz. To explain this, we model the emission as a well-mixed thermal/non-thermal plasma, as suggested by Condon et al. (1991). In this model the synchrotron spectrum is modified at low frequencies by thermal (free-free) absorption and we use the standard assumption of a 10% free-free emission contribution at 1.4 GHz. For rates of star formation per unit area below $10^3 M_\odot$ yr^{-1}kpc^{-2} free-free absorption is not important at 5 GHz. But, from the measured surface brightness of NGC 4418, we find that free-free absorption should indeed be a significant effect also at 5 GHz. This would naturally explain the shape of the spectrum and also the lack of radio emission at 1.4 GHz. From this modeling, we can also estimate the total star formation rate of the compact features detected in NGC 4418. Correcting for the possible absorption we get 7-70$M_\odot$ yr^{-1}kpc^{-2}, in good agreement with the 30-100$M_\odot$ yr^{-1}kpc^{-2} estimated by Sakamoto et al. (2013). Our conclusion is that although we cannot fully constrain the nature of the hidden power source in NGC 4418 there must be a significant starburst component.

6.1 Modelling radio emission of a well-mixed plasma

In the final part of Paper I, we use a model of radio emission from a well-mixed synchrotron and free-free emitting plasma presented by Condon et al. (1991). However, in contrast to the original model proposed by Condon et al. (1991) we do not model the radio emission as a function of turn-over frequency, but rather as a function of star formation rate per unit area. This change of parameter is very briefly summarized in the paper, but for the interested reader it might be useful to see a detailed derivation of how this was done. Therefore, I include below a derivation of how to relate the turn-over frequency in the model of Condon et al. (1991) to an actual star formation rate per unit area.

For NGC 4418, we can neglect cosmological effects and the observed flux density therefore scales with the distance d kpc as

$$F[\mathrm{W/Hz/m^2}] = \frac{L}{4\pi d^2 k^2}. \tag{6.1}$$

where k=$10^3 \cdot 3.09 \cdot 10^{16}$ is the conversion from kpc to meters. An area of size 1 kpc^2 at distance d kpc subtends an angular size

$$\theta^2[\mathrm{arcsec^2}] = \left(\frac{\mathrm{1kpc}}{d}\frac{180}{\pi}\cdot 60\cdot 60\right)^2 \tag{6.2}$$

This means that the observed surface brightness due to spectral luminosity L coming from an area 1kpc^2 is

$$S = \frac{F}{\theta^2} = \frac{\frac{L}{4\pi d^2 k^2}}{\left(\frac{1}{d}\frac{180}{\pi}\cdot 60\cdot 60\right)^2} \tag{6.3}$$

or

$$S[\text{mJy/arcsec}^2] = \underbrace{10^3}_{milli-} \cdot \underbrace{10^{26}}_{Jansky} \frac{\pi L[\text{W/Hz/kpc}^2]}{4k^2\,(180 \cdot 60 \cdot 60)^2}. \tag{6.4}$$

From Condon (1992) Eq. 6 together with the Tb-to-S conversion in the text after eq. 5 and the ν^2 scaling mentioned in eq. 5 we get

$$S_\nu[\text{mJy/arcsec}^2] = \left(\frac{\nu}{8.4}\right)^2 \cdot 10^{-1.3} \cdot T_e \cdot \left(1 - e^{-\tau}\right) \cdot \left[1 + 10\left(\frac{\nu}{1\text{GHz}}\right)^{(0.1-\alpha)}\right] \tag{6.5}$$

where $T_e = 10^4$K, $\alpha = 0.8$ and ν_c is the turn over frequency where the free-free optical depth equals 1, i.e. $\tau = (\nu/\nu_c)^{-2.1}$. Let us write this in a more compact form as

$$S_\nu[\text{mJy/arcsec}^2] = X \cdot \left(1 - e^{-\tau}\right) \cdot Y. \tag{6.6}$$

To relate the radio emission to the SFR, we only want to scale the optically thin part, i.e. ($\tau << 1$) in eq. 6.5. Using the first two terms in the Taylor series for the exponential function i.e.

$$e^x = 1 + x... \tag{6.7}$$

we can write

$$S_\nu[\text{mJy/arcsec}^2] = X \cdot Y \cdot \nu^{-2.1} \cdot \nu_c^{2.1} \tag{6.8}$$

Bell (2003) gives a relation between 1.4 GHz spectral luminosity of a star forming galaxy and its star formation rate:

$$\text{SFR}[M_\odot/\text{yr}] = A \cdot L_{1.4}[\text{W/Hz}]. \tag{6.9}$$

with $A = 5.52 \cdot 10^{-22}$. Since we are interested in surface *brightness*, we divide this by 1 kpc^2 to get:

$$\text{SFR}[M_\odot\text{yr}^{-1}\text{kpc}^{-2}] = A \cdot L_{1.4}[\text{WHz}^{-1}\text{kpc}^{-2}]. \tag{6.10}$$

We can now relate the star formation rate per unit area to the turn over frequency in the well-mixed thermal/non-thermal model. Putting everything together (assuming $\nu = 1.4$ in the formulas above) we get the relation

$$\text{SFR}[M_\odot\text{yr}^{-1}\text{kpc}^{-2}] \approx 172\nu_c^{2.1}. \tag{6.11}$$

This relation can be used to translate between a specific SFR to a critical frequency ν_c. Using this together with 6.5 we produced figure 5 in Paper I. We note that since we selected the SFR in powers of 10 instead of selecting turn-over frequency in powers of 10, the curves in our figure are not exactly the same as in the original figure by Condon et al. (1991).

6.2 Future work

Unfortunately, the data from 2001 were not good enough to fully constrain the nature of the power source in NGC 4418. We now know it cannot be only an AGN, but to find out which (if any) of the compact features we see that is associated with the AGN we need better image fidelity and better spectral information. Therefore, we applied for new observations, which were carried out in February and March this year. At the time of writing these lines we have not seen yet the new data, but we hope the quality is good enough to produce images with significantly lower noise, and to resolve the compact features also at 1.4 GHz.

Chapter 7

Outlook

All the projects presented in this thesis are continuing with future observations, as mentioned in the respective chapters. The preliminary results of the Arp220 monitoring and the M82 imaging are very promising and publications are planned based on these data. We also hope the recent observations of NGC 4418 were successful and that we will be able to follow up Paper I with a new publication to better constrain the nature of the compact features detected.

In addition to the projects mentioned in this thesis, I am also involved in the luminous infrared galaxy inventory (LIRGI) survey currently being observed by eMERLIN in the UK. LIRGI covers 42 of the most luminous LIRGs in the northern hemisphere. The sample was selected from the IRAS revised bright galaxy sample (Sanders et al. 2003) as sources with $\log(L_{IR}/L_{\odot}) > 11.4$, including the ULIRG Arp220. Most objects are mergers or post-mergers and are at distances < 200 Mpc. Unfortunately, the commissioning of eMERLIN has been delayed several times. However, during the writing of this thesis we received news that our first observations were carried out in late February and that we will get the first data in the end of March. By then, this thesis will be printed, but the analysis and observations will continue. This time we will not only get continuum images, we will also look for HI and OH emission and absorption lines. The LIRGI sample has also been observed with the EVN to find evidence for compact emission. This part of the project is also ongoing, and it is likely that I will be involved in calibration and imaging of these data in the future. We have also proposed a project to use images from the LOFAR MSSS survey to investigate the low-frequency spectra of our 42 LIRGI sources, as well as other bright galaxies in the IRAS bright galaxy sample. Preliminary calculations show that we should easily detect dozens of galaxies, providing useful information about the FIR/radio correlation at low frequencies. We hope this project will start during 2014 when the MSSS data have been fully commissioned.

We have also been granted International LOFAR observations to make high-resolution images of the galaxy NGC3079 using a technique similar to what we employed for imaging M82. We want to look at the nuclear starburst, the radio extensions seen with the GMRT, as well as the extended radio halo. These observations were completed on March 13th but we have yet to calibrate and image the data.

Finally we have applied for time with the international LOFAR baselines to observe Arp 220 with high resolution at low frequencies. We should resolve the two nuclei and be able to compare flux densities with images produced by eMERLIN with similar resolution at higher frequencies.

Appendix A

APPENDICES

A.1 Investigating amplitude discrepancies in VLBI data

While imaging VLBI data for the galaxy Arp 220 we found a discrepancy in the recovered flux density in images from the two epochs BP129, BB297A (correlated at Socorro) and the three epochs GC031A,B,C (correlated at JIVE), all C-band observations. The measured flux densities were significantly higher in the epochs correlated at JIVE than in Soccorro. To get a firmer hold on the difference, the noise levels in the UV-data were compared to theoretical estimates for all epochs. The discrepancy is clearly visible also in the scatter of the calibrated visibilities on specific baselines. The corrections derived by AIPS (APCAL using measurements of system temperature, TY, and telescope gain curves, GC) are similar for the different epochs (JIVE vs Socorro) indicating stable SEFDs of the telescopes. Hence the problem must be due to differences in the data coming into AIPS.

There clearly is a discrepancy between the JIVE and Socorro visibilities before the AIPS amplitude calibration APCAL stage. This difference is carried all the way through to the final images affecting the scientific interpretation. We are left with three important questions:

- Why is there a systematic difference between the correlators?
- Which correlator is correct?
- What is the correct system efficiency n_s for the two correlators?

We have carefully followed the instructions for calibration of JIVE and Socorro data. Still we might have made some mistake and we would be very grateful if this could be pointed out. Via e-mail, Bob Campbell of JIVE have commented our findings as: *[...] GC031a-c [C] were all observed [...] when we were still using the MkIV hardware correlator. When we were doing the MkIV/SFXC comparisons when bringing SFXC on-line, we were finding that the MkIV was giving higher amplitudes than SFXC. The MkIV amps were about 17% higher than those from SFXC or DiFX.* Since there is a known amplitude problem with data correlated at these times with the JIVE correlator, we are led to assume that JIVE is wrong and Socorro is correct. Hence, if we do not gain new knowledge before our coming paper is published, we will likely scale the JIVE data (down by 25-35%, see Table A.1) to the Socorro data.

In this document, we describe the investigations we have been doing to arrive at these conclusions.

A.1.1 Difference in recovered flux densities

The first test we did was to use all sources detected in all 5 C-band experiments BP129, GC031A,B,C and BB297A to derive correction factors for GC031A,B,C assuming BP129 and BB297A experiments were reliable. We chose this reference since at that point we didn't know what the EVN pipeline was doing since the link was broken to the pipeline scripts. The difference can be seen in tab. A.1. It is clear that the JIVE epochs are significantly brighter than the Socorro epochs. This test includes everything in the calibration and imaging of all the five epochs. To better find out the cause of this discrepancy, we decided to look at the distribution of the calibrated UV-data on a single baseline, see Sec. A.1.2.

Table A.1: Comparison of recovered flux densities for several sources in different epochs. The factors were derived selecting sources that were well detected at BP129 and BB297A-C, and resolved according to our criterion in Batejat et al. (2011) at all 4 GC031A,B,C and BB297A-C epochs. The flux density of these well resolved sources is expected to follow a linear decline over this period.

Epoch	Date	Correlator	Flux density in BB297A / flux density
BP129	09-JAN-2006	Socorro	1.0
GC031A	10-JUN-2008	JIVE	0.6103
GC031B	24-OCT-2008	JIVE	0.6657
GC031C	27-FEB-2009	JIVE	0.6753
BB297A	16-MAY-2011	Socorro	1.0

An example of the light curve (C-band in green) before and after correction can be seen for the bright compact source W34 in Fig. A.1.

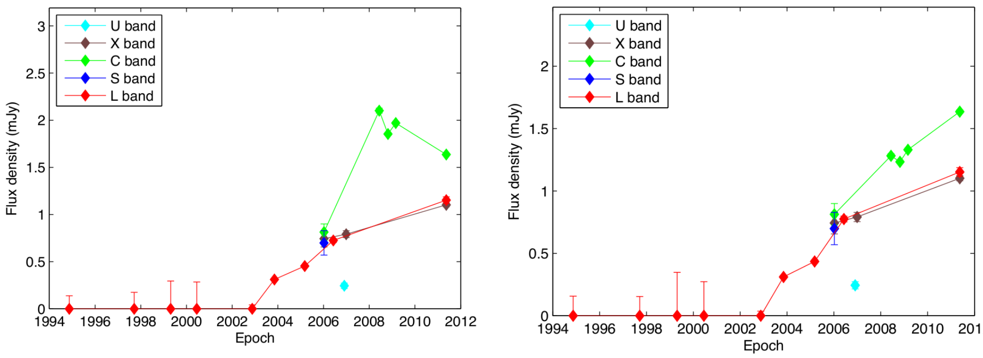

(a) (b)

Figure A.1: Example of light curves for one source, W34, before (a) and after (b) correcting for the systematic offset in visibility amplitudes.

A.1.2 Expected RMS noise of calibrated visibilities

The RMS noise for the real part of visibilities for a single polarization on a single baseline can be calculated as described in Romney (2012):

$$\sigma[\mathrm{Jy}] = \frac{\mathrm{SEFD[Jy]}}{n_s\sqrt{2Bt}}, \tag{A.1}$$

where n_s is the system efficiency, t is the integration time, B is the bandwidth. For 2-bit sampling of cross correlations we use n_s=1/1.68 (BFACTC=1.68 as tabulated in Kogan (1995)). **NOTE: This factor is not confirmed to be correct in these five epochs and must be treated with caution.** All epochs had integration time 2 seconds. Experiments BP129 and GC031C had 500kHz/channel bandwidth, while BB297A, GC031A and GC031B had 1MHz/channel bandwidth. In this document, all the analysis is performed on a single channel in the center of the total bandwidth, i.e. channel 10 in IF2.

Estimating the SEFD of antennas SC and OV

The most accurate way of estimating the SEFD is to look at the SN-solutions produced by APCAL from the Tsys and GC measurements for the actual experiment, see fig. A.2. In the selected time range we get SEFD(SC)≈ 19^2 =361 Jy and SEFD(OV)≈ 16.8^2 =282 Jy. For antennas with different SEFDs the value in Eq. A.1 can be replaced by the geometric mean according to Romney (2012):

$$\mathrm{SEFD} = \sqrt{\mathrm{SEFD_{OV}} \cdot \mathrm{SEFD_{SC}}} = \sqrt{282 \cdot 361} \approx 319\,\mathrm{Jy}. \tag{A.2}$$

The official specification for the VLBA antennas is on average SEFD=210 Jy, see Romney (2012). However: The VLBA's original 6 cm receivers are being replaced with substantially upgraded systems based on the EVLA design according to Romney (2012) and the SEFD of 210 is for the new receivers Romney (2012). The new receivers are about 35% better than the old ones, but were only available on Pie Town and Hancock as of 2012-01-05 Romney (2012). Hence, the SEFD in the GC031A and BB297A experiments should be 35% higher than 210 Jy, i.e. about $210/0.65 \approx 323$ Jy on average. This value is in excellent agreement with the measured geometric mean, see eq. A.2. We note also that the AIPS Cookbook, VLBA calibration recipe App. C.6 section 3a it says that VLBA antennas have SEFD near 300Jy at cm wavelengths, this probably meaning before the receiver upgrade.

Measured RMS noise levels of calibrated visibilities

Expected RMS noise of the calibrated visibilities were calculated for five C-band epochs using eq. A.1 and the values are summarized in Tab. A.2. Examples of

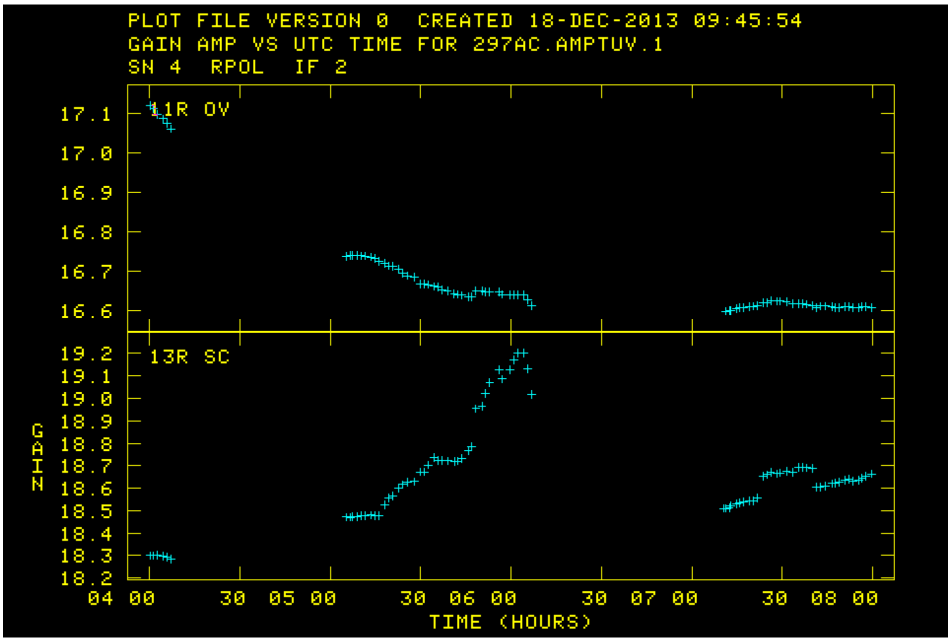

(a)

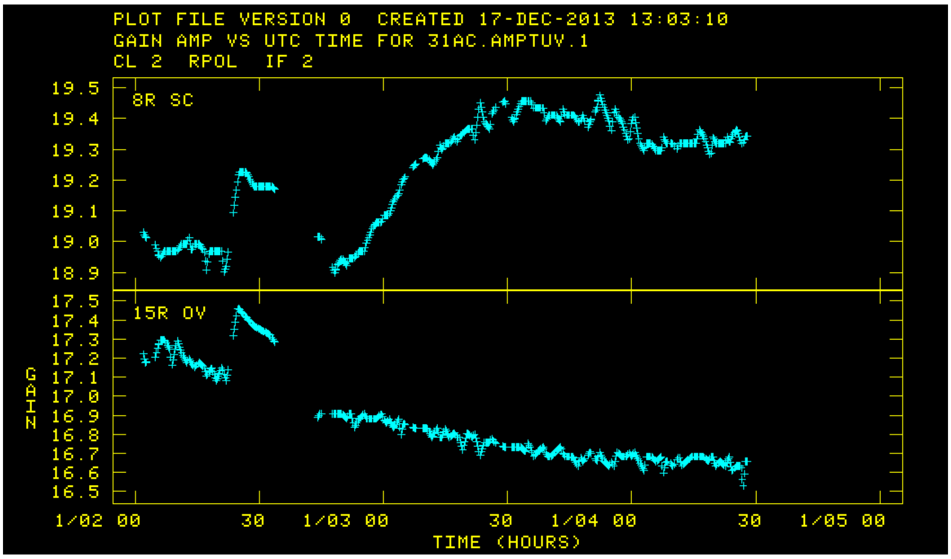

(b)

Figure A.2: APCAL corrections for BB297A and GC031A. For BB297AC we look at IF2 SN4 (SN1 and 2 was ACCOR + Smooth, SN3 APCAL, SN4 smooth APCAL). For GC031A ACCOR is not used and we use the pipeline calibration, and inspect CL2 from the EVN pipeline directly. We see that the values are very similar for the two epochs (note the reverse order of antennas in the two figures). In the selected time range we get SEFD(SC)$\approx 19^2$ =361 Jy and SEFD(OV)$\approx 16.8^2$ =282 Jy.

Gaussian fits to the data can be seen in Fig. A.3. The Gaussian distribution was defined as

$$\rho(\mu, \sigma) = Ae^{\frac{-(x-\mu)}{2\sigma^2}} \tag{A.3}$$

where x is the real part of the visibilities (horizontal axis in the histograms), A is the amplitude and μ is the mean (close to 0). We only give values for σ here since this is what is predicted by eq. A.1. The high value for GC031B compared to GC031A and GC031C could be due to calibration errors in this particular baseline in this time range for this dataset. As an extra cross-check, the same measurement was done for two another VLBA baseline KP-LA, showing a lower value for GC031B and otherwise consistent with the OV-SC results. Although different baselines are affected by different SEFDs during the experiment, the general trend that JIVE epochs are above Socorro epochs is still clear. However, perhaps this difference is due some error in the calibration process?

Table A.2: Comparison of predicted and measured RMS noise levels for calibrated data. Two baselines were analyzed, OV-SC and KP-LA. Note that the epochs BP129 and GC031C have higher theoretical values since the channel bandwidth is smaller for these epochs.

Epoch	Correlator	Theoretical RMS	OV-SC	OV-SC/ theory	KP-LA	KP-LA/ theory
BP129	Socorro	379	267	0.70	267	0.70
GC031A	JIVE	268	227	0.85	227	0.85
GC031B	JIVE	268	254	0.95	237	0.88
GC031C	JIVE	389	335	0.88	296	0.76
BB297A	Socorro	268	172	0.64	194	0.72

Checking amplitude calibration

We double checked all the calibration steps, making sure that DIGICOR=1 and ACCOR was used for the Socorro epochs, but not for the JIVE epochs. The test above used the EVN pipeline amplitude calibration. We re-did this for GC031A manually using ANTAB, and found the same corrections as the pipeline. Also the measured SEFDs, i.e. the APCAL-values (see fig. A.2), were similar. Hence, we trust that the correction from APCAL is not the problem. But, this means that the source of the discrepancy is earlier in the chain of events, i.e. in the uncalibrated data coming from the correlator. Our investigation of this continues in Sec. A.1.2.

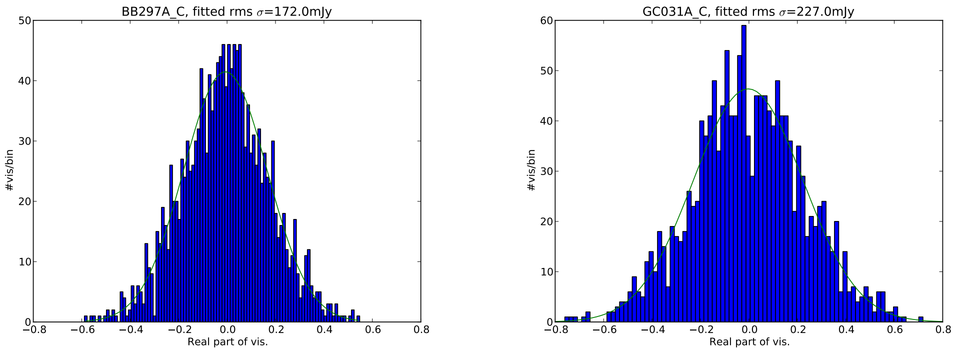

(a) (b)

Figure A.3: Example of two Gaussian fits to the real part of the final calibrated visibilities for the two epochs BB297A (left) and GC031A (right). Worth mentioning here is that these values were obtained without subtracting the final clean image, i.e. the Arp220 sources are still in these data. However, these are weak and tests made (not presented here) reveal that subtracting the final clean model only before doing the Gaussian fitting only makes a very minor difference to the noise levels measured here.

Measuring RMS noise of UNcalibrated visibilities

The RMS noise of the raw visibilities (before APCAL) should be the same as eq. A.1 without the SEFD correction, i.e.

$$\sigma = \frac{1}{n_s\sqrt{2Bt}}. \tag{A.4}$$

Expected RMS noise of the UNcalibrated (RAW) visibilities were calculated for five C-band epochs using eq. A.4 and the values are summarized in Tab. A.3. Examples of Gaussian fits to the data can be seen in Fig. A.4. To compare apples to apples, DIGICOR=1 and ACCOR has been applied to the Socorro data. We can still see the discrepancy noted earlier. It seems to be a problem in the correlation products, not in the pipeline or APCAL-calibration. Comparison with the measured values will show if the discrepancy measured in the flux densities and RMS noise is present also in the raw data coming from the correlator. We note that $1/\sqrt{2} \approx 0.707$ and that $1/2^{0.25} \approx 0.841$.

A.1.3 Conclusions

To compare the original values in tab. A.1, derived from the images, to the ratios derived for visibilities (with different channel widths for different epochs) we introduced the label K in tab. A.3. The values for K(BB297A)/K in tab. A.3 and the ratios in tab. A.1 show a clear difference carrying all the way through

Table A.3: Comparison for uncalibrated data, i.e. using DIGICOR=1 in FITLD when loading Socorro datasets and applying ACCOR to the Socorro data. Note that the epochs BP129 and GC031C have higher values since the channel bandwidth is smaller for these epochs.

Epoch	Correlator	Theoretical RMS	Measured OV-SC	K=Measured/ theory	K(BB297A)/K
BP129	Socorro	1.19	0.83	0.70	0.93
GC031A	JIVE	0.84	0.71	0.85	0.76
GC031B	JIVE	0.84	0.71	0.85	0.76
GC031C	JIVE	1.19	1.02	0.85	0.76
BB297A	Socorro	0.84	0.55	0.65	1.0

from the uncalibrated visibilities to the final calibrated images. From tab. A.2, we see that the JIVE data is closest to the theoretical values given by eq. A.1. Even though the theoretical values are uncertain because of poor knowledge of n_s, the ratio of recovered flux densities in the final images can still be explained as a difference in the correlator output. We find it very likely that the jump we see in the light curves is in fact due to a discrepancy between the JIVE and Socorro correlators. If we do not gain new knowledge before our coming paper is published, we will scale the JIVE data (down by 25-35%, see Table A.1) to the Socorro data.

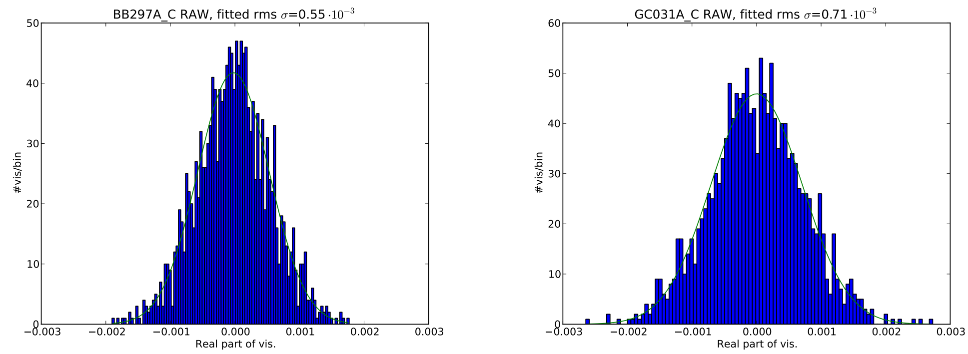

(a) (b)

Figure A.4: Example of two Gaussian fits to the real part of the uncalibrated visibilities for the two epochs BB297A (left) and GC031A (right). Note that DIGICOR=1 and ACCOR has been applied to BB297A, these corrections should already have been applied by the JIVE correlator.

A.2 Comparison of methods for size estimation

Batejat et al. (2011) developed a statistical test to measure sizes of the compact sources detected in Arp 220. This method is based on comparing the apparent size in the image with a model convolved to the same resolution. To account for possible effects on noise the method is statistical in the sense that the comparison is carried out on many (thousands) of random source-free positions on the map. This method is good, but in principle it would be even better to fit a model directly to the calibrated visibilities, i.e. the data coming from the interferometer. To find out if we could improve our results by using visibility fitting, and to get a systematic check of the accuracy of the image based method developed by Batejat et al. (2011), we performed model fitting to the visibilities of several epochs of VLBI observations of Arp220. The Fourier-model fitting was carried out using version 2 of the UV-multifit software currently under development as described by Marti-Vidal et al. (2014). The model assumed was a spherical shell with the inner shell surface having 30% of the width of the outer shell. For optimal convergence the fitting was limited to a maximum shift from the peak position of 2 mas, a maximum possible diameter of 6 mas and a maximum flux density of 3 mJy. The results were plotted to investigate manually by eye if the fit made sense, and two examples can be seen in Fig. A.5. We find three main conclusions:

- Because of better relative weighting of the visibilities when imaging compared to when fitting in Fourier space, the noise is lower in the former and we find more sources above our detection limit using the image based method. The possibility of more elaborate relative weighting could in principle be added to the Fourier model-fitting code, but such an extension is beyond the scope of this thesis.
- The sizes derived from the two methods are in good agreement, see Fig. A.6(b), although the measurements have large error-bars in both methods.
- The flux densities derived from the two methods show a systematic offset, where the Fourier-based method finds less flux than the image based method, see Fig. A.6(a). This is probably again due to the difference in weighting between the two methods, or to the CLEAN bias effect (giving too high flux values in the image due to deconvolution errors).

In the end, we concluded that the image fitting produced good results for more sources since the weighting could be chosen to obtain higher signal to noise also for weaker sources. Future analysis of size and flux densities of compact sources in Arp220 will likely be performed using the image based method.

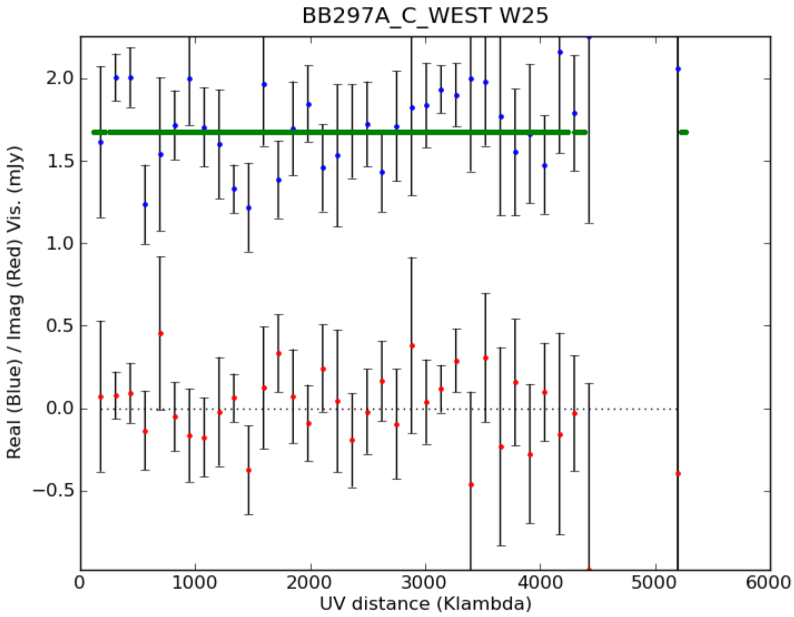

(a)

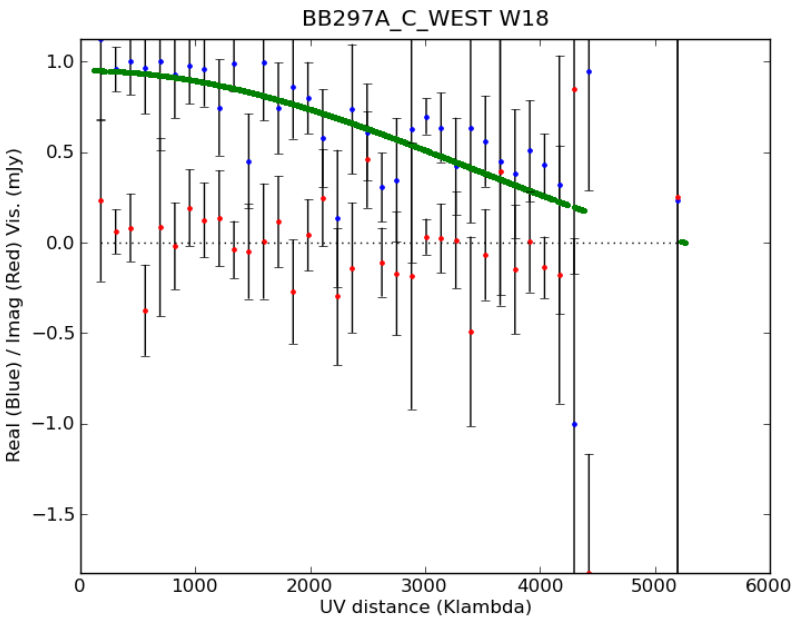

(b)

Figure A.5: Example results of model-fitting a spherical shell in Fourier space to data from epoch BB297A at 5 GHz. The results are plotted as radially averaged bins of real and imaginary parts of the calibrated visibilities, together with the fitted model. The imaginary part is plotted to make sure that no unintended shift of the model position with respect to the data was introduced, which would show as clear non-zero structure in the imaginary part. In Fig. (a) we show the data and best fitted model for W25, one of the brightest sources detected. By eye we find its Fourier transform to be essentially flat, i.e. a point source, which is also what we obtained from the fit. In Fig. (b) we see W18, an older source which is clearly extended, with a fitted size of 1.4 mas.

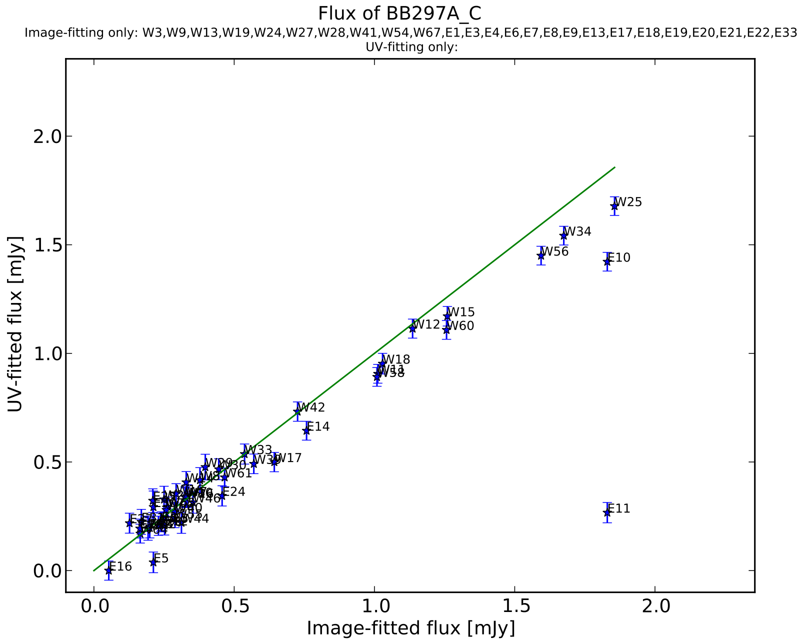

(a)

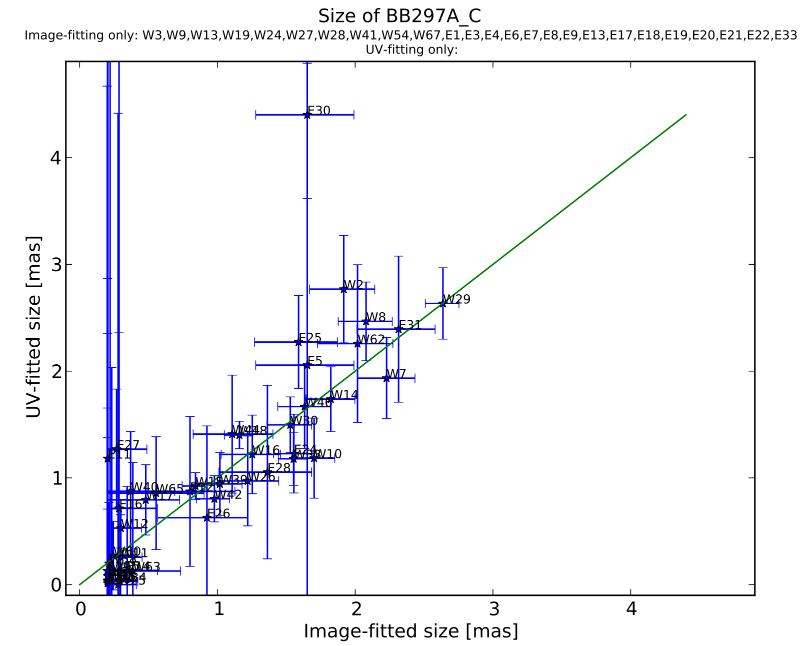

(b)

Figure A.6: Results of comparing two methods to measure the flux (a), and size (b) of the sources seen in with VLBI Arp220 in experiment BB297A at 5.0GHz. Many sources are only detected when using the image based method and are therefore excluded from these plots. The horizontal axis shows the values obtained with the image based approach, and vertical axis the Fourier-based approach.

A.3 Description of data and calibration of M82 with LOFAR

These data were taken in project LC0_026 (P.I.: J.E. Conway) observed in two parts: 10 hours taken during the night between the 20th and 21st of March 2013 and 6 hours taken in the evening of April 5th 2013. The observations were split in two to maximize the hour angle coverage during night time. Three objects, J0958+6533, M81 and M82, were observed simultaneously using three beams. Every hour the observations switched to a single beam on 3C196 for 2 minutes. Positions assumed for correlation of each source are listed in Tab. A.4.

3C196 was observed to anchor the absolute flux scale of the observations. The observations of 3C196 could also be used to phase-up core stations, something which was not done in this work. J0958+6533 (known to be 0.74 Jy at 74 MHz in VLSS; Cohen et al. (2007)) was observed to estimate delay, rate and phase corrections at an angular distance of 3.5° from M81 and 4.1° from M82. M81 was observed as a close (0.61° from M82) phase calibrator.

All four linear polarization products (XX, XY, YX, YY) were correlated. Data were taken in 8-bit HBA joined mode, where the available total bandwidth of 96 MHz was divided equally between the three objects M81, M82 and J0958+6533, each covering the same range in frequency. The single beam on 3C196 covered the same 32 MHz. The observed 32 MHz bandwidth was divided in two segments of 15820.3125 kHz each, one centered on 117.967224 MHz and one centered on 153.904724 MHz. However, the lower part was found hard to calibrate and the rest of this paper only describes the analysis of the upper 16 MHz. After correlation the data was stored in the LOFAR long term archive (LTA) as measurement sets (MS) with channel width 3051.758 Hz and integration time 1.0 seconds, in the form of 81 sub-bands with 64 channels each. We estimate that with these data it is possible to phase-rotate (shift) the visibilities to image regions up to $10'$ away from M82 with less than 3% coherence loss at the longest international baselines. In this paper no such phase-rotation was applied since we were only interested in the central regions of M82.

In addition to the high-resolution data, the data was also averaged in time and frequency by the LOFAR pipeline and stored in the LTA with channel width 48828.125 Hz and integration time 2.0 s. This data was also run through the LOFAR pipeline flagger to automatically identify and edit bad data. Because of the custom requirements involved in processing data including international baselines the averaged and flagged data were downloaded (~ 3.2 TB) to computers at Onsala Space Observatory. Local copies of the LOFAR software NDPPP as well as the Astronomical Image Processing System (AIPS) release 31DEC13 (Greisen 2003), ParselTongue v2.0 (Kettenis et al. 2006) and CASA v3.4 (McMullin et al. 2007) were installed. At Onsala data were further averaged using NDPPP to a channel bandwidth of 195.3125 kHz (i.e. 81 channels in total) and 10.0 s integration time. This was done to reduce data volumes, and we estimate

Table A.4: List of correlated positions for each target

Source	R. A. [J2000]	Dec. [J2000]
3C196	08h13m36.0000s	+48°13′03″.000
J0958+6533	09h58m47.2451s	65°33′54″.818
M81	09h55m33.1731s	69°03′55″.062
M82	09h55m51.5500s	69°40′45″.792

the coherence loss due to time and frequency smearing to be less than 3% for the longest international (1158km; van Haarlem et al. (2013)) baselines for emission at an angular distance of 30″ from the phase center. Similarly, we estimate the coherence loss to be less than 3% for the longest remote baselines (121km) at an angular distance of 5′.

Both the March and April observations included the same 44 LOFAR high band array (HBA) stations. These were 23 core stations (CS): CS001, CS002, CS003, CS004, CS005, CS006, CS007, CS011, CS017, CS021, CS024, CS026, CS028, CS030, CS031, CS032, CS101, CS103, CS201, CS301, CS302, CS401, CS501, eight international (INT) stations: DE601, DE602, DE603, DE604 (no fringes detected, see below), DE605, FR606, SE607, UK608 and 13 remote stations (RS): RS106, RS205, RS208, RS305, RS306, RS307, RS310, RS406, RS407, RS409, RS503, RS508 and RS509. No formation of super-stations by, for example, adding the CS together was done.

A.3.1 Correcting for residual delay, rate and phase

Because of residual rates affecting international baselines we need to derive rate corrections using a global fringe-fitting algorithm. This has not yet been implemented within the LOFAR software packages, nor in CASA. Therefore, we decided to use AIPS for calibrating these data.

To be readable in AIPS the data were converted from linear to circular polarization using the tool *mscorpol* v1.6, developed by Tobia Carozzi at Onsala Space observatory, and converted to UVFITS format using the task *exportuvfits* in CASA. In AIPS the task FIXWT was used to re-compute the relative weights of all visibilities to the inverse square of the standard deviation within 5 minutes of data. After adjusting the weights the data were divided into 4 minute scans.

The global fringe fitting algorithm (Thompson et al. 2001, see) as implemented in AIPS task FRING does only solve for a single residual delay within each intermediate frequency (IF) present in the data. At low radio frequencies the residual delay due to the ionosphere might vary considerably as a function of frequency. Since these data cover a large fractional bandwidth (10.3%, solving for one single delay over the full 15.8 MHz might leave significant delay errors.

To mitigate this effect, the 81 channels were split in three IFs of 27 channels each, using the task MORIF.

Corrections for residual delays and rates of all stations with respect to the core were derived using J0958+6533. The search were restricted to baselines longer than 75kλ, a search window of 600 ns and one solution every 2 minutes. Solutions were found separately for each IF and polarization. Since all CS are close and share a common clock, no corrections were needed for the core stations, only for the INT and RS. Typical residual delays were found to be 100-300 ns, and typical residual rates were 1-3 mHz. The corrections were smoothed using a median window filter with support time 30 minutes before applied to the data. An example of a fringe detection showing the good signal to noise on the longest baseline between France and Sweden can be seen in Fig. A.7. The difference in residual delay between the lowest and highest of the three IFS were typically 10-15 ns for the international stations.

Bad data were edited using UVFLG in AIPS. No fringes were detected to DE604 and this station was not used at all.

A.3.2 Anchoring the absolute flux scale to 3C196

After correcting for delay and rate, the task CALIB was used to derive amplitude and phase corrections for J0958+6533 assuming this source to be a 0.5 Jy point source at the phase center. A solution interval of 4 minutes was used, and the two circular polarizations were averaged together. The flux density of J0958 was chosen iteratively to give the right flux density for 3C196 expected from literature, see below. J0958 is compact, but there are other strong (500 mJy) sources nearby (4.7′). To avoid contamination from these sources disturbing the amplitude calibration only baselines $> 75k\lambda$ were used when determining amplitude corrections, thereby excluding CS-CS, RS-RS and CS-RS baselines. After calibration, imaging using task IMAGR in AIPS recovered 505 mJy flux density using baselines $> 75k\lambda$ (CLEAN beam 0.41″×0.26″, pixelsize 0.02″, σ1.1 mJy/beam) in good agreement with what was specified. But, when imaging using baselines between 2 and $75k\lambda$ (i.e. excluding baselines to INT stations as well as CS-CS; CLEAN beam 5.17″×4.37″, pixel size 0.5″, σ =0.34 mJy/beam) a total flux density of 681 mJy was recovered with a peak of 557mJy/beam. This can be compared to the integrated flux density obtained with the VLSS of 740 mJy (CLEAN beam 80″) Cohen et al. (2007). It seems J0958+6533 is resolved at INT baselines even though no structure is visible. All integrated flux densities were obtained summing pixels brighter than 3σ. All imaging was done using Briggs Briggs (1995) robust 0 weighting.

After applying the corrections derived for J0958 to 3C196 imaging could be improved by re-calibrating the phases of the 3C196 visibilities, because of the large angular separation (22°). The CS and RS could be calibrated assuming a

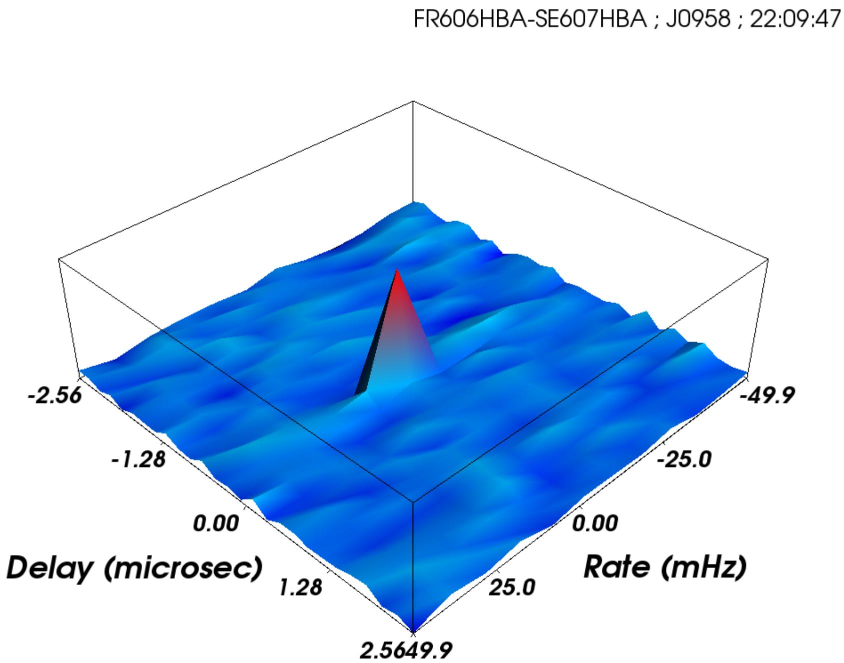

(a)

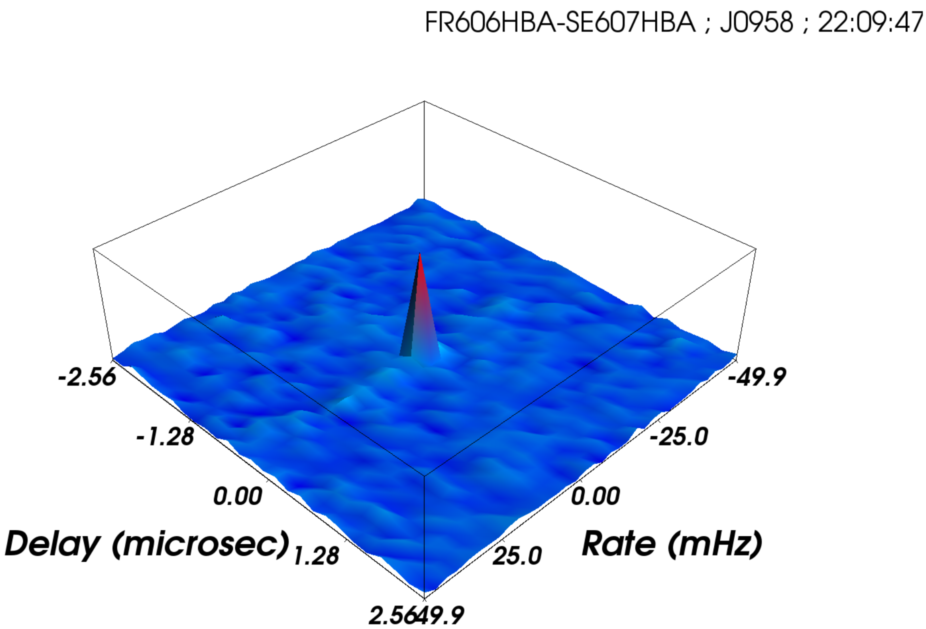

(b)

Figure A.7: Delay-rate plots using one IF (5.2MHz) of calibrated data for the source J0958+6533. Fig. (a) is using 2 minutes of data, i.e. the same length used for finding the delay and rate corrections using FRING. Fig. (b) is using 6 minutes of data, which gives better resolution in the rate direction. These few minutes of data were selected for the longest possible LOFAR baseline from France to Sweden, or in terms of station names: FR606HBA - SE607HBA. We clearly see that we have enough signal to noise to derive delay and rate corrections on this baseline within 2 minutes using this 500 mJy source. The claibrated peak is well centered at zero in both delay and rate.

point source model deriving one solution for each 2 min scan. The corrections were found using baselines in the range 0.1 to $75k\lambda$ (excluding the shortest CS baselines as well as INT baselines). The two polarizations were averaged together but each IF were solved for separately. Imaging (0.1-75kλ, cell size 0.2″, CLEAN beam 7.84″×6.18″, σ =0.3 Jy/beam) reveals 3C196 to be partially resolved, see Fig. A.8.

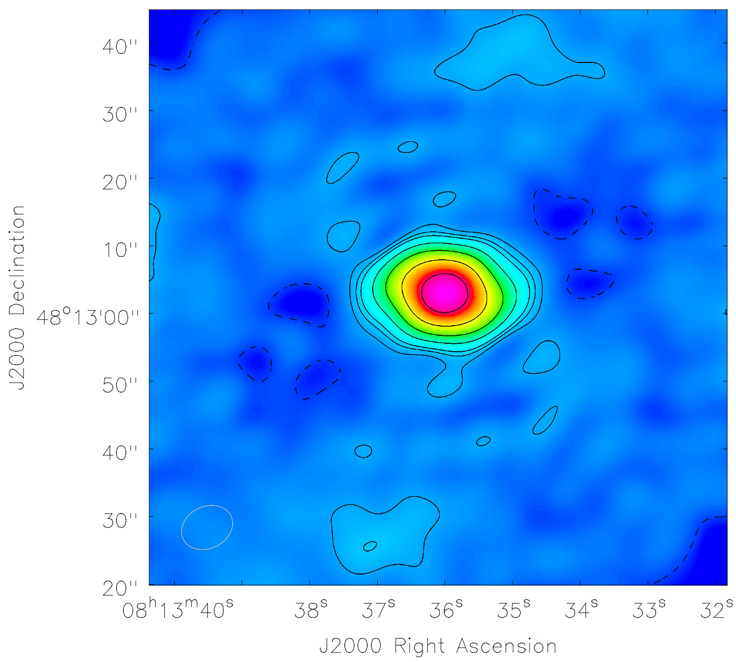

Figure A.8: Deconvolved image of the flux calibrator 3C196 with noise RMS σ =0.222 Jy/beam. Contours at (-3, 3, 6, 9, 20, 40, 80, 160)×σ. We clearly see that 3C196 is resolved, although we cannot see the individual components in this image. The beam of size 7.84″×6.18″ is shown in the bottom left corner. We note the relatively faint but symmetric imaging artifacts, indicative of minor errors in the amplitude calibration.

The final integrated flux density recovered for 3C196 was 87.9 Jy, in good agreement with the 89.9 Jy expected from interpolating measurements from the literature at other MHz frequencies, see Fig. A.9. Because of the limited Fourier sampling (16×2 min) we were not able to properly calibrate the INT station visibilities for 3C196. However, this was not necessary to obtain the integrated flux density to set the flux scale as described above. We estimate the absolute flux calibration to be accurate to within 10%.

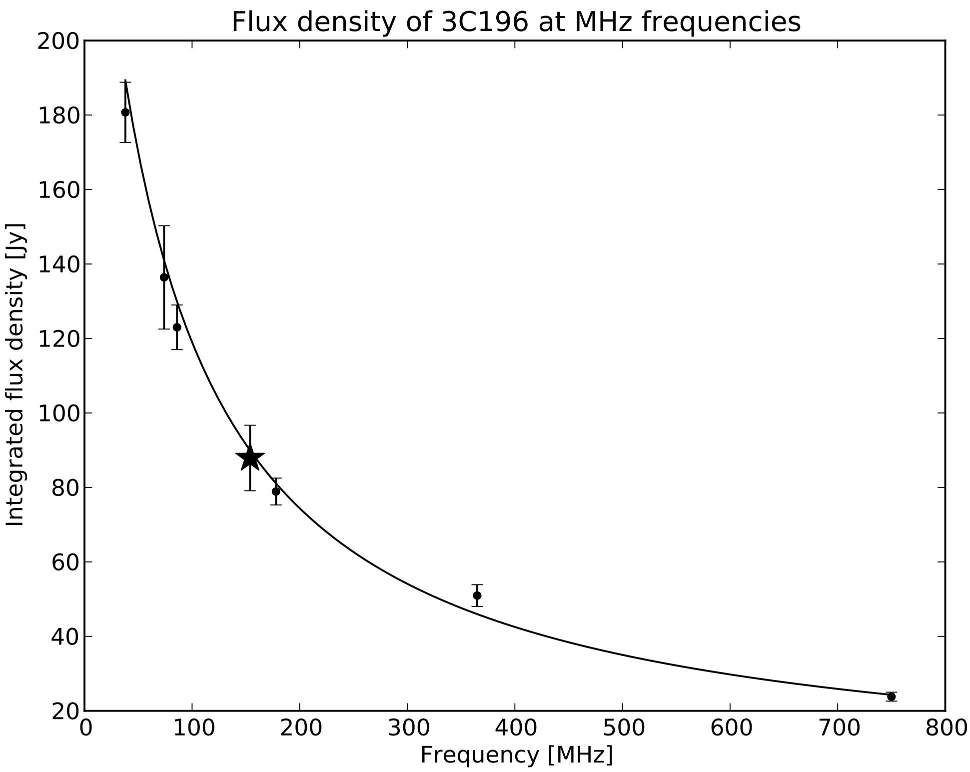

Figure A.9: Several measurements of 3C196 at MHz frequencies are plotted together with the flux density 87.9 Jy recovered from these LOFAR observations (marked with a star). The other measurements are: 136.40±13.88 Jy at 74 MHz (Kassim et al. 2007), 123.0±6 Jy at 86 MHz (Laing et al. 1980), and the remaining four taken from (Kuehr et al. 1981); 80.71±8.1 Jy at 38 MHz, 78.9±3.6 Jy at 178 MHz, 50.96±2.92 at 365 MHz and 23.8±1.2 at 750 MHz. Fitting a trend of $1/\nu$ we expect to find 89.9 Jy at 154 MHz, in good agreement with what we measure.

A.3.3 Refining the phase calibration for M81 and M82

The cumulative corrections derived for J0958+6533 (delay, rate, amplitude and phase) were transferred to M81. Because of the 3.5° angular separation between J0958 and M81 the visibility phases were re-calibrated on M81 assuming a point source model. Corrections were derived every 2 minutes, using baselines $>$ $75k\lambda$ and averaging over IFs and polarizations.

A deconvolved image from IMAGR using baselines $> 75k\lambda$ (CLEAN beam 0.43″×0.26″, pixel size 0.03″, σ0.14 mJy/beam) recovers a point source of 46.0 mJy.

A deconvolved image from IMAGR using baselines between 2 and $75k\lambda$ (CLEAN beam 5.02″×4.08″, pixel size 0.5″, $\sigma = 0.20$ mJy/beam) recovers 87.5 mJy associated with the point source M81 (peak 57.0 mJy/beam).

M82 was now imaged with international baselines only ($> 75k\lambda$, CLEAN beam 0.41″×0.25″, cell size 0.03″, σ =0.13 mJy/beam) using the cumulative corrections derived for M81, at angular separation 0.61°. To refine the phase calibration further, phase-only self-calibration was done using the image of M82 itself. The total flux density in clean components used for self-calibration of M82 was 62.72 mJy. Corrections were derived once every 5 minutes, averaging over IFs and polarizations. After applying the phase corrections derived from self-calibration the data were converted once more to MS for imaging in CASA. Finally, the task CLEAN in CASA required the MS mount type to be updated to X-Y for all antennas using *taql* before deconvolution.

A.3.4 Imaging of compact structure

The compact emission was imaged using only baselines longer than $75\,\mathrm{k}\lambda$ and cell size 0.02″. This gave a resolution (CLEAN beam) of 0.387″×0.242″. Since only compact structure was present the multi-scale option was not used here. Two Taylor terms were used, but we also deconvolved once using only one Taylor term which revealed almost identical results. From deconvolution of stokes V we estimate the minimum (thermal) image noise to be 0.165 mJy/beam. The deconvolved stokes I image (see Fig. 5.1) has image RMS noise 0.166 mJy/beam, indicating that we successfully deconvolved all the emission down to the thermal noise limit. Figure 5.1 is, to our knowledge, the highest resolution image ever made at this and lower frequencies.

A.3.5 Imaging of extended structure

Before imaging the extended structure, the model obtained through deconvolution of the compact structure (see Sect. A.3.4) was subtracted from the data using the task UVSUB in AIPS. The extended emission was now imaged from the uvsubtracted data by using only baselines of length between 0.1 and $75\,\mathrm{k}\lambda$

and cell size 0.5″, giving a resolution (CLEAN beam) of 5.33″×4.39″. The multi-scale option was used, and the scales were selected as the geometric series 0, 20, 40, 80, 160 pixels. The largest scale correspond to the largest scale expected for the core (Adebahr et al. 2013, ∼1′). From deconvolution of stokes V we estimate the minimum (thermal) image noise to be 0.16 mJy/beam. The deconvolved stokes I image (see Fig. 5.2) has image RMS noise 0.44 mJy/beam, indicating that we did not successfully deconvolve all the emission present. The Further improvement of the image fidelity by, for example, using different deconvolution algorithms on these data might be possible, but are beyond the scope of this work.

M82 itself has a peak flux density of 165.3 mJy/beam and an integrated flux density of 11.878 Jy (summing the pixels associated with M82 above 3σ in Fig. 5.2). In addition, there is ∼100 mJy (above 3σ) in Fig. 5.1 which was UV-subtracted before making Fig. 5.2. The total flux density of M82 at 154 MHz is therefore 12.0±1.2 Jy. There is a significant difference in brightness between the central region and the ring of emission surrounding it. The minimum brightness inside the ring (in the middle hole) is 62.4 mJy/beam, less than half the peak brightness of the ring.

Polarized emission?

There is a weak (peak 2.23 mJy/beam) signal in stokes V tracing the brightest part of the extended emission visible in the stokes I image. This fraction ($\sim 1\%$ of stokes I) is too small to be visible above the noise when imaging the compact emission in stokes V. Brief investigations reveal a similar fraction of emission in stokes V relative to stokes I for the calibration sources J0958 and M81. Since the polarizations were averaged together in the calibration process, any Polarized signal must either be real or due to some error before the calibration. A proper polarization calibration of these data is beyond the scope of this work and will not change the stokes I measurements presented here. The signal visible in stokes V for M82 could, for example, be due to leakage in the LOFAR receivers, or some minor error when converting from linear to circular polarization. Another possible explanation of the V Stokes signal in the LOFAR data could be differential R/L absorption by the ionosphere, because of the orientation of the Earth's magnetic field relative to the incoming radiation. However, this has to be investigated in more detail.

Bibliography

Adebahr, B. et al. (July 2013). In: *A&A* 555, A23, A23. DOI: 10.1051/0004-6361/201220226. arXiv:1209.5552 [astro-ph.GA].

Armus, L., T. M. Heckman, and G. K. Miley (Mar. 1988). In: *APJL* 326, pp. L45–L49. DOI: 10.1086/185120.

Batejat, F. et al. (Oct. 2011). In: *APJ* 740, 95, p. 95. DOI: 10.1088/0004-637X/740/2/95. arXiv:1109.6443 [astro-ph.CO].

Bell, E. F. (Apr. 2003). In: *ApJ* 586, pp. 794–813. DOI: 10.1086/367829. eprint: astro-ph/0212121.

Berezhko, E. G. and H. J. Völk (Nov. 2004). In: *A&A* 427, pp. 525–536. DOI: 10.1051/0004-6361:20041111. eprint: astro-ph/0408121.

Briggs, Daniel Shenon (1995). PhD thesis. The New Mexico Institute of Mining and Technology.

Brunthaler, A. et al. (May 2009). In: *A&A* 499, pp. L17–L20. DOI: 10.1051/0004-6361/200912327. arXiv:0904.2388 [astro-ph.CO].

Chevalier, R. A. (July 1982). In: *ApJ* 258, pp. 790–797. DOI: 10.1086/160126.

— (Oct. 2007). In: *Supernova 1987A: 20 Years After: Supernovae and Gamma-Ray Bursters*. Ed. by S. Immler, K. Weiler, and R. McCray. Vol. 937. American Institute of Physics Conference Series, pp. 206–211. DOI: 10.1063/1.2803564. eprint: astro-ph/0612734.

Cohen, A. S. et al. (Sept. 2007). In: *AJ* 134, pp. 1245–1262. DOI: 10.1086/520719. arXiv:0706.1191.

Condon, J. J. (1992). In: *ARAA* 30, pp. 575–611. DOI: 10.1146/annurev.aa.30.090192.003043.

Condon, J. J. et al. (Sept. 1991). In: *ApJ* 378, pp. 65–76. DOI: 10.1086/170407.

Costagliola, F. et al. (Aug. 2013). In: *AAP* 556, A66, A66. DOI: 10.1051/0004-6361/201220634. arXiv:1306.2211 [astro-ph.GA].

Draine, B. T. and D. T. Woods (Dec. 1991). In: *ApJ* 383, pp. 621–638. DOI: 10.1086/170820.

Gendre, M. A. et al. (May 2013). In: *MNRAS* 431, pp. 1107–1120. DOI: 10.1093/mnras/stt231. arXiv:1209.6478 [astro-ph.CO].

González-Alfonso, E. et al. (May 2012). In: *A&A* 541, A4, A4. DOI: 10.1051/0004-6361/201118029. arXiv:1109.1118 [astro-ph.CO].

Greisen, E. W. (Mar. 2003). In: *Information Handling in Astronomy - Historical Vistas* 285, p. 109. DOI: 10.1007/0-306-48080-8_7.

Kassim, N. E. et al. (Oct. 2007). In: *ApJS* 172, pp. 686–719. DOI: 10.1086/519022. arXiv:0704.3088.

Kettenis, M. et al. (July 2006). In: *Astronomical Data Analysis Software and Systems XV*. Ed. by C. Gabriel et al. Vol. 351. Astronomical Society of the Pacific Conference Series, p. 497.

Kogan, L. (Dec. 1995). VLBA Scientific MEMO no. 12. URL: https://science.nrao.edu/facilities/vlba/publications/memos/sci/index/sci12memo.pdf.

Kuehr, H. et al. (Sept. 1981). In: *A&AS* 45, pp. 367–430.

Lacki, B. C. (June 2013). In: *MNRAS* 431, pp. 3003–3024. DOI: 10.1093/mnras/stt349. arXiv:1206.7100 [astro-ph.CO].

Lacki, B. C., T. A. Thompson, and E. Quataert (July 2010). In: *ApJ* 717, pp. 1–28. DOI: 10.1088/0004-637X/717/1/1. arXiv:0907.4161 [astro-ph.CO].

Laing, R. A. and J. A. Peacock (Mar. 1980). In: *MNRAS* 190, pp. 903–924.

Lonsdale, C. J. et al. (Aug. 2006). In: *ApJ* 647, pp. 185–193. DOI: 10.1086/505193. eprint: astro-ph/0604570.

Maiolino, R. et al. (Oct. 2003). In: *MNRAS* 344, pp. L59–L64. DOI: 10.1046/j.1365-8711.2003.07036.x. eprint: arXiv:astro-ph/0307380.

Marti-Vidal, I. et al. (Jan. 2014). In: *ArXiv e-prints*. arXiv:1401.4984 [astro-ph.IM].

McMullin, J. P. et al. (Oct. 2007). In: *Astronomical Data Analysis Software and Systems XVI*. Ed. by R. A. Shaw, F. Hill, and D. J. Bell. Vol. 376. Astronomical Society of the Pacific Conference Series, p. 127.

Roche, P. F. et al. (Jan. 1986). In: *MNRAS* 218, 19P–23P.

Romney, Jon (Jan. 2012). Online at NRAO. URL: http://www.vlba.nrao.edu/astro/obstatus/2012-01-06/.

Sakamoto, K. et al. (Feb. 2013). In: *APJ* 764, 42, p. 42. DOI: 10.1088/0004-637X/764/1/42. arXiv:1301.1878 [astro-ph.CO].

Sanders, D. B. et al. (Oct. 2003). In: *AJ* 126, pp. 1607–1664. DOI: 10.1086/376841. eprint: arXiv:astro-ph/0306263.

Smith, H. E. et al. (Jan. 1998). In: *ApJ* 493, pp. L17–L21. DOI: 10.1086/311122.

Taylor, G. B., C. L. Carilli, and R. A. Perley, eds. (1999). Vol. 180. Astronomical Society of the Pacific Conference Series.

Thompson, A Richard, James M Moran, and George W Swenson (2001). Weinheim: Wiley-VCH.

van Haarlem, M. P. et al. (Aug. 2013). In: *A&A* 556, A2, A2. DOI: 10.1051/0004-6361/201220873. arXiv:1305.3550 [astro-ph.IM].

Wills, K. A. et al. (Nov. 1997). In: *MNRAS* 291, p. 517.

Yun, M. S., N. A. Reddy, and J. J. Condon (June 2001). In: *ApJ* 554, pp. 803–822. DOI: 10.1086/323145. eprint: arXiv:astro-ph/0102154.